ARTICLES
https://doi.org/10.1038/s41551-020-00612-w

nature biomedical engineering

Decoding of facial strains via conformable piezoelectric interfaces

Tao Sun[1,6], Farita Tasnim[1,6], Rachel T. McIntosh[1,2], Nikta Amiri[3], Dana Solav[1,4], Mostafa Tavakkoli Anbarani[3], David Sadat[1], Lin Zhang[1], Yuandong Gu[5], M. Amin Karami[3] and Canan Dagdeviren[1]✉

Devices that facilitate nonverbal communication typically require high computational loads or have rigid and bulky form factors that are unsuitable for use on the face or on other curvilinear body surfaces. Here, we report the design and pilot testing of an integrated system for decoding facial strains and for predicting facial kinematics. The system consists of mass-manufacturable, conformable piezoelectric thin films for strain mapping; multiphysics modelling for analysing the nonlinear mechanical interactions between the conformable device and the epidermis; and three-dimensional digital image correlation for reconstructing soft-tissue surfaces under dynamic deformations as well as for informing device design and placement. In healthy individuals and in patients with amyotrophic lateral sclerosis, we show that the piezoelectric thin films, coupled with algorithms for the real-time detection and classification of distinct skin-deformation signatures, enable the reliable decoding of facial movements. The integrated system could be adapted for use in clinical settings as a nonverbal communication technology or for use in the monitoring of neuromuscular conditions.

Human skin allows for an abundance of fine muscular movements that form the ability to communicate in daily life, whether through shaping vocal sounds into recognizable speech or through forming facial expressions for nonverbal communication[1–3]. Despite the importance of facial movements, much is still unknown about the quantifiable patterns of mechanical deformation that occur on the skin as a result of the contraction and relaxation of muscles. Precise measurements of soft tissue biokinematics, such as skin strain during facial deformations, can be used to computationally recognize distinct facial motions and, therefore, facilitate nonverbal communication for patients who lack the ability to speak or interact using traditional electronic communication interfaces.

Many neuromuscular disorders, such as amyotrophic lateral sclerosis (ALS), are caused by peripheral nerve degeneration, interruptions in the signalling and response pathways between motor neurons and muscles, and eventual muscular atrophy[4]. Although these diseases have low prevalence and incidence, they induce severe disability and high fatality rates; 50% of patients with ALS die within 15–20 months after diagnosis[5]. Such disorders often manifest themselves through physiological changes in a person's hands, feet and other body parts, including gradual loss of their ability to exercise fine motor skills and to vocalize intelligible speech[6]. As a result, patients with ALS or related disorders experience barriers to tasks that require finger dexterity and sustained speech, but often retain the ability to form facial motions[7]. Predictable methods for continuously tracking dynamic skin strain on the face can therefore enable new forms of communication for individuals with such disorders.

At present, methods for in vivo characterization of facial deformations often involve electromyography[8,9] or camera tracking[10–17]. Although these systems provide valuable insights into the characterization of facial motions, capturing such measurements typically results in cumbersome computational load or requires the use of rigid, bulky structures with highly visible interfaces to soft skin, presenting a difficulty for continuous use in daily life, especially for individuals with neuromuscular disorders (Supplementary Table 1). As such, present technologies are often unsuitable for continuous, portable monitoring or for use on highly curvilinear regions of the body, such as the face. An alternative strategy involves the use of thin film piezoelectric materials, such as lead zirconate titanate (PZT)[18–20], $BaTiO_3$ (ref. [21]) and zinc oxide (ZnO)[22], or fibre forms of the copolymer of polyvinylidene fluoride with trifluoroethylene[23,24], to convert changes in soft tissue strain to measurable changes in electrical voltage and current. Such piezoelectric thin film devices have been increasingly explored for biomedical sensors, transducers and energy harvesters[25,26] because they can be tailored to offer (1) high dynamic sensitivity across a wide pressure regime (0–100 kPa), (2) simplicity in device structure, (3) reliability and (4) stability under cyclic loading conditions[18,27,28]. However, a widely deployable system for real-time detection of facial motions would further necessitate the use of low-cost materials, easily manufacturable processes, and a seamless pipeline for fabrication, testing and validation.

Here we introduce a set of materials, device designs, fabrication steps, theoretical calculations, simulations and validation protocols that realize robust, mechanically adaptive, predictable and visually invisible (Supplementary Video 1) in vivo monitoring of spatiotemporal epidermal strains as well as decoding of distinct facial deformation signatures through the use of conformable devices comprising aluminium nitride (AlN) piezoelectric thin films on compliant polydimethylsiloxane (PDMS) substrates. The use of a substrate with an elastic modulus that is comparable to that of the human epidermis enables soft reversible lamination of the

[1]Media Lab, Massachusetts Institute of Technology, Cambridge, MA, USA. [2]Department of Electrical Engineering and Computer Science, Massachusetts Institute of Technology, Cambridge, MA, USA. [3]Department of Mechanical and Aerospace Engineering, University at Buffalo, Buffalo, NY, USA. [4]Faculty of Mechanical Engineering, Technion Israel Institute of Technology, Haifa, Israel. [5]Institute of Microelectronics, Agency for Science, Technology and Research (A*STAR), Singapore, Singapore. [6]These authors contributed equally: Tao Sun, Farita Tasnim. ✉e-mail: canand@media.mit.edu

conformable facial code extrapolation sensor (cFaCES) onto any area of skin, permitting rapid, repeatable measurements of skin strain during facial motions without causing any inflammation and/or allergic reactions while remaining stable across a range of temperatures and humidities on the human skin[18,29–32] (Supplementary Fig. 1). We further present a methodology that enables voltage–strain correlation in mechanically adaptive, piezoelectric devices and informs their placement by quantitative study of dynamic soft tissue biokinematics using stereophotogrammetry (PG) and subsequent three-dimensional digital image correlation (3D-DIC). This methodology generates accurate, repeatable spatiotemporal maps of full-field facial skin strains and device-on-skin strains during facial movements. Comprehensive theoretical and in vitro experimental studies established that these systems can provide accurate and reproducible measurements of strain during compression, stretching and bending in quasistatic regimes. Similar characterization of the sensor on a mock skin set-up suggests enhanced sensor sensitivity when coupled with soft, elastomeric targets. Preliminary in vivo experiments on healthy individuals and patients with ALS coupled with further theoretical studies and 3D-DIC assessment demonstrate that the predictability, reproducibility and sensitivity of skin strain measurements using cFaCES enable real-time decoding (RTD) and classification of an individual's facial motions, potentially enabling an alternative method of nonverbal communication for individuals with neuromuscular disorders, such as ALS.

Sensor development

Figure 1a,b provides images and schematics of the cFaCES. Fabrication of the cFaCES (Supplementary Fig. 2) followed by an electrical anodization process (Supplementary Fig. 3) achieves the sensor's conformable structure, which yields seamless integration with facial skin (Supplementary Fig. 4). The ultrathin architecture of the active piezoelectric elements, along with the serpentine metal electrodes that establish their electrical connections, result in low elastic modulus, conformable structures when supported by a thin elastomer (PDMS; thickness, 40 μm) substrate. The lateral configuration of the cFaCES consists of an array of AlN thin films, which demonstrate anisotropic growth (0002) of wurtzite crystal structure (Supplementary Fig. 5) patterned in circular shapes, enabling localized spatiotemporal measurements of strain without directional bias. The circular structures are capacitor-type elements, each of which incorporates a layer of AlN (thickness, 1.5 μm; diameter, 0.48 cm) sandwiched between two molybdenum (Mo) electrodes (200 nm) and encapsulated with a layer of silicon dioxide (SiO_2; thickness, 1 μm). cFaCES has a simplified structure—that is, a 2 × 2 spatial array of piezoelectric elements—to reduce the amount of data processing that is required during RTD in an effort to push the boundary of the decoding accuracy with lower cost and lower computational load (Supplementary Table 1). Further fabrication details are provided in the Methods. Although any piezoelectric material could be incorporated in a cFaCES as the active layer without giving up functionality, the specific use of AlN fabricated in a 200-mm wafer process results in a low-cost (US$10 per cFaCES) disposable device (Supplementary Fig. 6a). The sensor achieves a response time (5 ms) that is fast enough to track the changes in muscle motions, which occur on 10 ms timescales (Supplementary Fig. 6b). Furthermore, the complementary metal–oxide–semiconductor (CMOS)-compatible nature[33–35] of the AlN piezoelectric layer can enable mass manufacturability, while the lead-free property of the device materials can make the clinical transition much smoother, when compared to a device with lead-based piezoelectrics, such as PZT, especially in countries in which lead-based devices are being actively phased out of production[36,37]. Owing to the minimal thickness of all of the component layers[38,39], the resulting device can be applied conformally and securely to the skin with the use of a thin 3M Tegaderm medical tape (thickness, 40 μm) with an adhesion force of ~1.5 N and adhesion strength of ~60 N m^{-1} (Supplementary Fig. 6c), and is stable over a wide temperature range (25–65 °C; Supplementary Fig. 6d). In vitro studies using human epidermal keratinocytes demonstrated the biocompatibility of the device. Particularly, cell-viability studies revealed no evidence of cell toxicity and the cell culturing process did not alter the surface properties of the sensor (Supplementary Fig. 7).

Biokinematic assessment of dynamically deforming soft tissue

The key to achieving highly predictable operation of the aforementioned localized sensor in vivo requires accurate voltage–strain correlation for any sensor placement location, and is realized by reliable, non-contact full-field spatiotemporal measurements of surface strains with and without cFaCES laminated onto the epidermal region of interest. Figure 1c provides a schematic of the custom-built system for PG and 3D-DIC for measuring the full-field spatiotemporal facial skin strain. When an object, such as the human face, is positioned in view of a set of cameras—such that each pair of two adjacent cameras has an overlapping field of view of the object—the cameras can reliably capture 12-bit-resolution images of the object's movement at a rate of 6 frames per second. If the object is speckled with a random pattern of dots (Supplementary Fig. 8) and then undergoes deformation during this image capture, subsequent multicamera 3D-DIC using MultiDIC[40,41] can accurately reconstruct the surface of the object in 3D space and track the strain field across that surface during movements. Sets of images collected from both a cylindrically shaped calibration object and a flat chequerboard distortion-correction object (Supplementary Fig. 9) were utilized to derive the intrinsic and extrinsic camera parameters (that is, focal lengths, principal point coordinates, radial and tangential distortion parameters, and skew parameters, position and orientation of the camera with respect to the global coordinate system) using both the direct linear transformation and bundle adjustment methods[40]. The determined direct linear transformation parameters and bundle adjustment parameters were then used to map two-dimensional (2D) image points of the calibration object into 3D space and calculate the reconstruction errors—which result from a variety of sources, such as image quality, focus and lighting. The presented set-up consistently produces root-mean-square (r.m.s.) reconstruction errors of approximately 100 μm, which characterizes the calibration of the set-up (Supplementary Figs. 10 and 11 and Supplementary Note 1a).

The 3D-DIC process includes analysis of pairwise images to detect matching image points and calculate their correlation coefficient, which is a parameter that describes the degree of 'matching' of the speckles on the object of interest as seen from two adjacent cameras (spatially) and as they move over time (temporally; Supplementary Note 1b). The calculation of correlation coefficients is the main result of 2D-DIC, and is computed using NCorr[42,43], the methodology of which defines a correlation cost function for which a lower degree of matching equates to a higher correlation coefficient. After the correlation process, 3D reconstruction followed by strain calculation results in a spatiotemporal full-field measurement of strain across the surface of the object of interest. Each pair of cameras produces a triangular mesh created from the 3D point cloud that is resolved from the 3D reconstruction of 2D image points (Supplementary Note 1c). The full-field displacements, deformations and strains are then calculated from the temporal changes in the 3D coordinates of the triangular mesh from each pair using a variation of the triangular Cosserat point element method[40,44,45] (Supplementary Note 1d). The eigendecomposition of the local Lagrangian strain tensor provides principal strain directions and magnitudes on each local surface element comprising the triangular mesh (Supplementary Note 1d). Throughout this paper, we follow the convention that the first principal strain is the

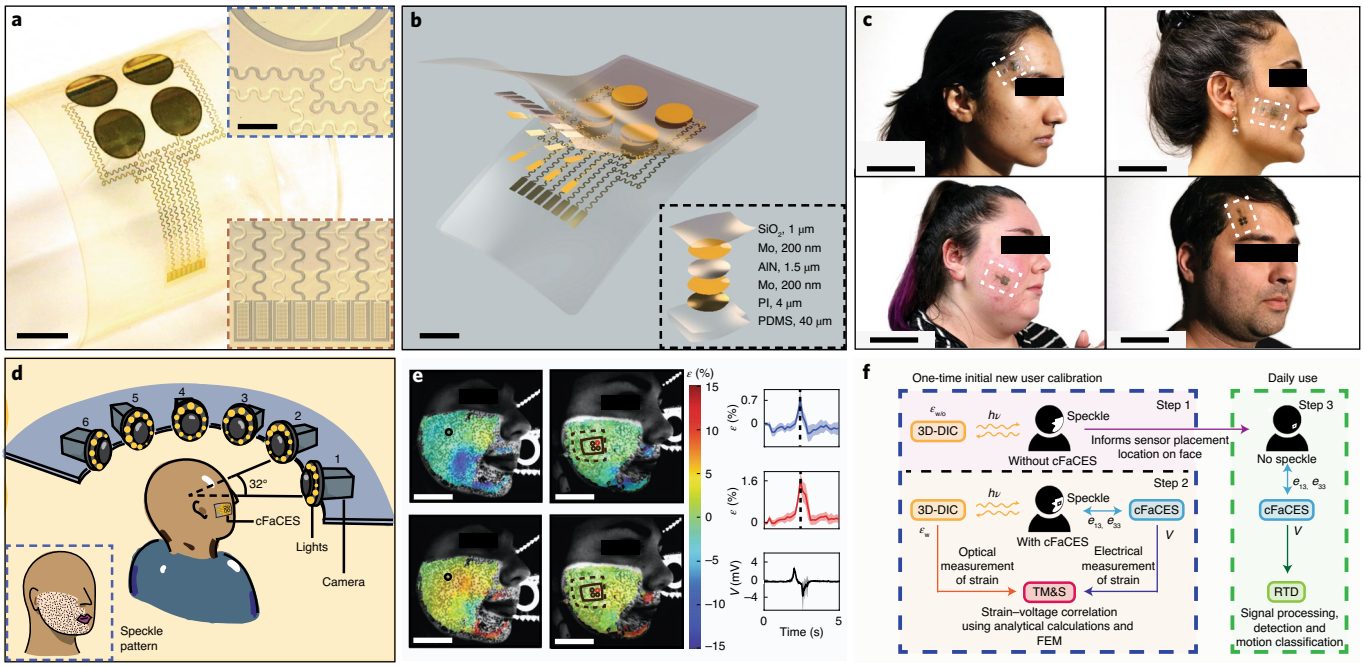

Fig. 1 | The system overview accompanying cFaCES. cFaCES is a system that involves measurements by (1) a conformable sensor for the real-time detection of facial motions through electrical responses to localized strains and (2) a non-contact PG + 3D-DIC set-up for determining full-field mechanical strains on the face using multicamera optical imaging. **a**, The conformable sensor laminated onto a curved glass cylinder. Scale bar, 5 mm. Insets: the edge of the AlN sensing element and its top and bottom Mo serpentine electrodes (top right); and the set of eight serpentine electrodes from four sensing elements connecting to Al bonding pads (bottom right). Scale bar, 1 mm (applies to both insets). **b**, Exploded view of a cFaCES, including each layer that encapsulates the sensing elements (bottom right inset). Scale bar, 5 mm. **c**, The cFaCES (white dashed box) laminated onto various participants in different locations of the face, such as on the cheek and temple. Scale bars, 5 cm. **d**, Schematic of the PG + 3D-DIC set-up showing the concept of 3D reconstruction of the face using an array of cameras with overlapping fields of view. Random speckling of the face (bottom left) is required to enable image point matching, resulting in reliable 3D reconstruction and subsequent calculation of skin strain that occurs during epidermal deformations. **e**, Skin strain and sensor voltage output were analysed while participants performed facial motions, such as right cheek twitch. The images on the left show strain maps as an example of the results from 3D-DIC trials of a human participant with the sensor (left) and without the sensor (right), showing minimal principal strain (top) and maximal principal strain (bottom). The solid boxes in the right two images indicate the location of the cFaCES; the solid circles indicate its four active elements; and the dashed box indicates the Tegaderm tape. The black circle in the left two images indicates the area of the skin on top of which the cFaCES element of interest was located during DIC trials with the sensor laminated on the face. The strain scale (%) is given on the right of the strain maps. The three graphs on the right show minimal principal strain (top, blue) and maximal principal strain (middle, red) measured on the top layer of the cFaCES (adhered to skin with Tegaderm tape) using 3D-DIC, and the resultant voltage output (bottom, black) from one (red circle) of the four sensor elements. For each period of 5 s, the averaged strain across the DIC-generated triangles ($n = 21$) corresponding to the sensing element from which voltage is measured is represented as a solid line, and the shaded band indicates s.d. In all of the DIC-generated images presented in this paper, the eyes of the participants were blocked with black boxes to maintain privacy. Scale bars, 5 cm. **f**, Flow chart of the key elements of the system. The system, after a one-time initial calibration period for a new user, can be used as a daily nonverbal communication tool without further calibration. Step 1: the patient's bare facial skin was speckled and optical (hv) measurement of strain ε without cFaCES ($\varepsilon_{w/o}$) was conducted while the patient formed various natural facial motions to inform later placement of the cFaCES on the facial skin. This step helped to maximize distinguishability between distinct motions. Step 2: after laminating the cFaCES onto the patient's cheek or temple, speckling was applied to the facial skin and optical (hv) measurement of strain ε with cFaCES (ε_w) was conducted simultaneously with electrical measurement of the voltage output (V) of the cFaCES, which occurs through the e_{13} and e_{33} modes of piezoelectricity. The two methods of strain measurement are connected by bimodal (analytical calculations and FEM) theoretical modelling and simulation (TM&S) to achieve voltage–strain correlation. This helped to achieve predictable RTD performance in vivo. Step 3: the cFaCES was laminated onto the face, as informed by the analysis of contour maps generated using 3D-DIC in step 1, and the piezoelectrically generated voltage waveforms underwent signal processing, detection and motion classification.

minimal in-plane strain; the second principal strain is the maximal in-plane strain occurring in an orthogonal direction; and the third principal strain—or out-of-plane strain—is immeasurable. Strain data gathered during DIC trials show the in-plane strain occurring on the top surface of the object of study. Control null-strain tests (Supplementary Fig. 12) give representative errors that result from the DIC set-up, data collection procedure and effect of analysing real human skin, and allow for reliable and theoretically predictable results for tracking the strain of facial skin and of the sensor laminated onto facial skin. Figure 1d shows a representative spatial map of the strain field at the peak strain time point during a human participant's right-cheek twitch motion. First (minimal) and second (maximal) principal surface strains are shown for a healthy individual performing the motion without (left) and with (right) a cFaCES laminated onto their cheek. Together with cFaCES electrical measurement when laminated onto different participants and in various locations of the face (Fig. 1e), 3D-DIC optical measurement of strain can be analysed using theoretical modelling to achieve predictable and verifiable strain-to-voltage correlation for the cFaCES devices. The 3D-DIC methodology, which is implemented only once during an initial calibration period for a new user, enables complex preanalysis of the human epidermis to be conducted, which can then translate to smarter device design and informed location selection for device placement onto the skin, so as to

maximize decodability from minimal sensing elements and data processing (Supplementary Fig. 1f).

Mechanical characterization and theoretical modelling

Measurements on controlled, uniaxial buckling, tensile (stretching) and compressive stages with an Instron (MicroTester 5948) machine (Fig. 2a) revealed that the cFaCES has quasistatic mechanical properties as a bare sensor in addition to when coupled with mock skin with a thickness of 2 mm (Dragon Skin, Smooth-On), so as to simulate in vivo behaviour when laminated onto human skin. Figure 2 displays the results of uniaxial buckling and stretching of a cFaCES laminated onto a mock skin. The neutral mechanical plane (NMP) of the cFaCES is located within 110 nm of the midplane of the piezoelectric active layer (Fig. 2b and Supplementary Note 2). Including the use of Tegaderm tape for application onto human skin shifts the NMP negligibly, maintaining it within the aforementioned range (Supplementary Fig. 13). Cyclic tests of cFaCES buckling with buckling centreline in the middle of the piezoelectric array and for buckling distances up to 8 mm (radius of curvature (ROC) = 1 mm) show negligible (<200 μV) peak-to-peak voltage outputs (Supplementary Fig. 13d). For buckling distances of 2 mm of the bare sensor (ROC = 3 mm) with the buckling centreline through two of the piezoelectric elements, the maximum strain experienced by the cFaCES piezoelectric element during in vitro trials was only 0.0185%, resulting in maximum voltages of ~200 μV (Supplementary Fig. 14). Given that the maximum strain allowable on wurtzite phase AlN is ~0.09% (ref. [46]), the minimum ROC—for buckling with centreline through two of the piezoelectric elements—that the cFaCES can support is 834 μm (Supplementary Note 2). This property of the cFaCES fixes its steady-state voltage output to ~0 V regardless of the initial curvature of the object on which it is placed, which is critical for a device that can be used predictably by a wide variety of individuals. The strain distributions and voltage outputs as predicted by theoretical calculations quantitatively characterize the nature of deformations that occur on the cFaCES as a bare sensor when buckled (Supplementary Fig. 14a) or stretched (Supplementary Fig. 14b) and when coupled with a mock skin and the resultant structure is buckled (Fig. 2d) or stretched (Fig. 2e). For cyclic compression, similar studies were conducted for the sensor on mock skin with and without Tegaderm tape (Supplementary Fig. 15a,b) as well as for the bare sensor (Supplementary Fig. 15c). The voltage outputs of the cFaCES as a result of the aforementioned cyclic deformation conditions at a variety of amplitudes are displayed in these figures, revealing that they are similar to predictions from two theoretical modalities—finite element model (FEM) simulations and analytical calculations.

For development of the voltage–strain correlation system, mechanical behaviours and voltages determined experimentally by cyclic, controlled deformation patterns of buckling, stretching and compression of the cFaCES, whether bare or coupled with a layer of mock skin, were predicted using an analytical model. Buckling behaviour is inherently nonlinear, and the partial differential equation governing the vibrations of post-buckled piezoelectric beams[47–52] is similar to the equations of buckling for a unimorph beam[48]. Derived by combining those of a buckled beam[53] and a piezoelectric energy harvesting bimorph[54,55], the governing equation for buckling of piezoelectric beams is as follows:

$$m\frac{\partial^2 w}{\partial t^2} + c\frac{\partial w}{\partial t} + EI\frac{\partial^4 w}{\partial x^4} + \left[P - \frac{EA}{2L}\int_0^L \left(\frac{\partial w}{\partial x}\right)^2 \mathrm{d}x\right]\frac{\partial^2 w}{\partial x^2} + \alpha\left[\frac{\mathrm{d}\delta(x)}{\mathrm{d}x} - \frac{\mathrm{d}\delta(x-L)}{\mathrm{d}x}\right]V(t) = 0 \quad (1)$$

where m is the total mass per unit length of the beam, w (which is a function of x and t) is deflection along the z axis, c is the damping coefficient, EI is the equivalent bending stiffness of the composite beam (with E as the Young's modulus and I as the moment of inertia), P is the axial load applied by the material testing system, EA is the equivalent axial stiffness of the beam (with E as the Young's modulus and A as the cross-sectional area), L is the length of the beam, α is the piezoelectric coupling coefficient, $\delta(x)$ is the Dirac delta function and $V(t)$ is the voltage across the piezoelectric element. If the width of the beam is noted by b the thickness of the substrate by t_s the thickness of the piezoelectric layer by t_p and the transverse piezoelectric coefficient by e_{13}, the piezoelectric coupling coefficient is then $\alpha = 2be_{13}\frac{t_s+t_p}{2}$.

The continuous equations of motion are discretized using the assumed-mode method, and the buckling mode shapes are taken to be the same as the vibration mode shapes of a pinned–pinned beam. The axial force applied by the Instron is larger than the first critical load but not the critical load of the higher modes. We therefore consider only the fundamental mode shape of buckling[53,56,57]. The fundamental mode shape of the simply supported beam is $\phi(x) = A\sin\left(\frac{\pi x}{L}\right)$ and the deflection of the beam can be written as a function separable in space and time, $w(x,t) = \phi(x)T(t)$, where A is an arbitrary constant and the function $T(t)$ governs the time dependence of beam deflection. The differential equations governing the vibrations of the first mode of coupling are:

$$\begin{cases} M\ddot{T} + c\dot{T} + (K-p)T + NT^3 + \beta V(t) = 0 \\ C_0\dot{V} + \frac{V}{R} = -\beta\dot{T} \end{cases} \quad (2)$$

where the modal mass is $w(x,t) = \phi(x)T(t)$ (the mass-normalized mode shapes are used), the linear stiffness coefficient is $K = EI\int_0^L \phi^{(4)}\phi\,\mathrm{d}x = A^2EI\frac{\pi^4}{2L^3}$, the damping of the beam is characterized by c which is related to the damping ratio as $K = EI\int_0^L \phi^{(4)}\phi\,\mathrm{d}x = A^2EI\frac{\pi^4}{2L^3}$. The reduction of the stiffness

Fig. 2 | In vitro mechanical characterization of the cFaCES on a mock skin. Voltage output resulting from uniaxial buckling and stretching of the cFaCES placed onto a mock skin set-up served as a first-order controlled approximation of the expected behaviour of the sensor on human skin. **a**, An optical photograph of the test set-up on the Instron machine shows the clamping of the cFaCES system, whether bare or on a mock skin. From the unperturbed state, one end of the system was either pushed closer, resulting in buckling behaviour, or pulled away, resulting in tensile stretching behaviour. The electrical output generated by the four sensing elements of the sensor is carried by an anisotropic conductive film cable that is connected to a printed circuit board (PCB), which is then connected by a shielded coaxial cable to the DAQ system. **b**, The NMP, $y_{neutral}$ (black dashed line), of a cFaCES is located in the middle of the piezoelectric layer, as shown in the cross-section drawing (green dashed box). **c**, The FEM simulates a single sensing element (red dashed box) as a current source I_p in parallel with a capacitor $C_p = 807$ pF, which mimics the piezoelectric charge-generating behaviour. To accurately predict the voltage values measured from the sensor, the DAQ system (blue dashed box) was included in the model as a parallel combination of a resistor and capacitor ($R_s = 1\text{M}\Omega \,||\, C_s = 265$ pF) connected to the two-wire output of the piezoelectric element. **d**,**e**, Voltage outputs from one sensing element as observed experimentally and predicted by analytical models and FEMs, in addition to strain fields predicted by the FEM, are shown for the case of buckling (BMS) (**d**) and stretching (SMS) (**e**) motions for the sensor-on-mock-skin system. The time scale is the same for all of the graphs in **d** and **e**. Deformation and strain fields are shown in the deformed configuration for the highest axial displacements for buckling (10 mm) and stretching (3.5 mm). The outline of the undeformed cFaCES–mock-skin system is shown by the thin grey wireframe in each strain map. The deformation (mm) and strain (%) scale for each strain map is given on the right. Scale bars, 2 cm.

coefficient due to the axial force is $p = -P\int_0^L \ddot{\phi}\phi \mathrm{d}x = AP^2\frac{\pi^2}{2L}$, the nonlinear coefficient is $N = -\frac{EA}{2L}\int_0^L (\dot{\phi})^2 \mathrm{d}x \int_0^L \ddot{\phi}\phi \mathrm{d}x = A^4 EA\frac{\pi^4}{8L^3}$, the coupling coefficient is $\beta = \alpha[\phi(0) - \phi(L)] = -2\alpha A\frac{\pi}{L}$ and the total capacitance of the piezoelectric layer is $\beta = \alpha[\phi(0) - \phi(L)] = -2\alpha A\frac{\pi}{L}$.

If the axial force is larger than the critical force, which leads to buckling, p will be larger than K and, according to Lyapunov stability theory, in that situation, the zero deflection equilibrium becomes unstable. However, this condition creates two new static equilibrium points located at $T = \pm\sqrt{\frac{p-K}{N}}$. The deflection of the beam results in the decrease in its length. If the uniform axial deformation is neglected compared with the geometric effects, the shortening of the beam is $T = \pm\sqrt{\frac{p-K}{N}}$. The governing differential

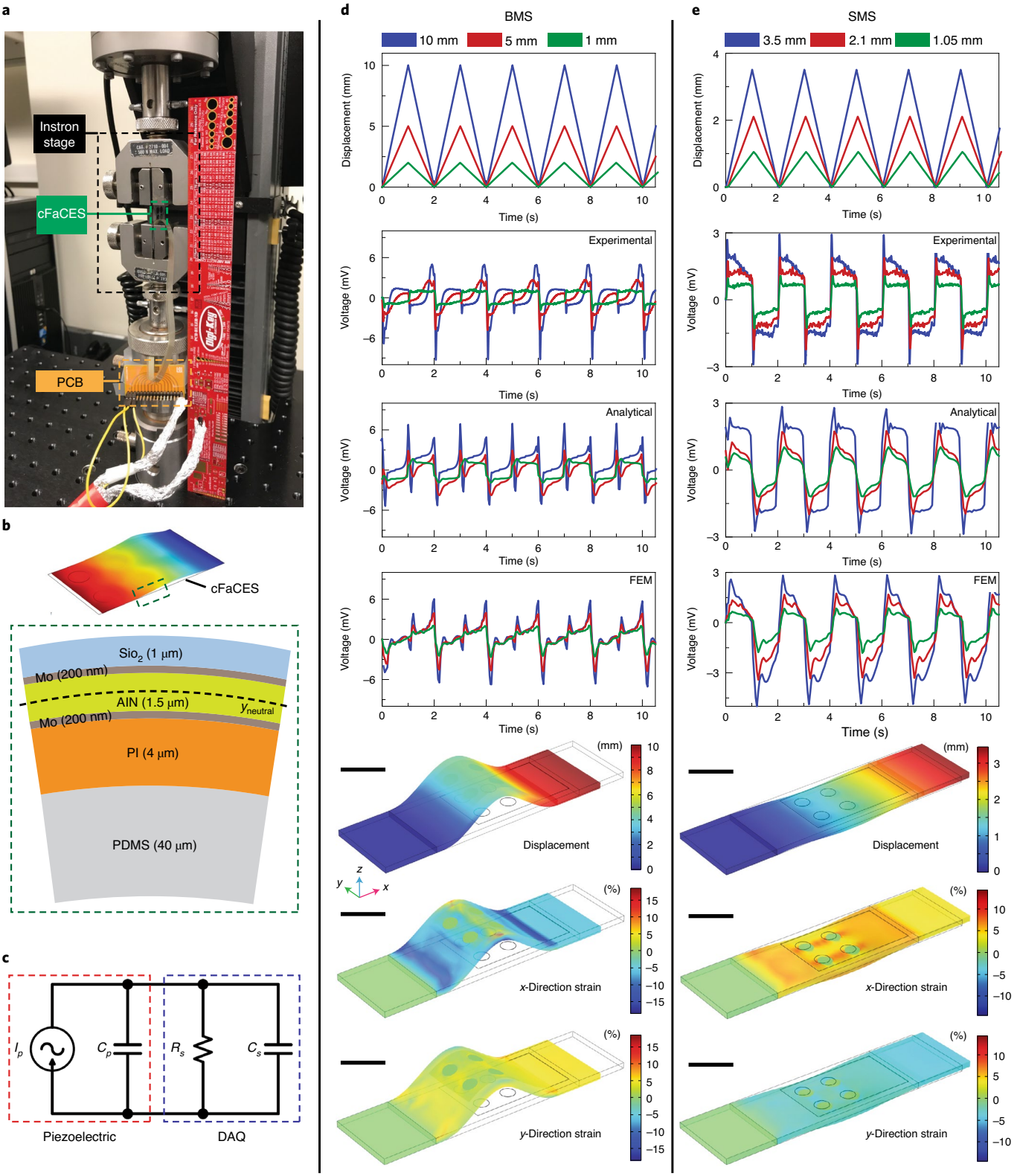

equations in equation (1) are valid when the axial load is controlled or known; however, in some of the tests, the axial displacement was controlled instead, for which a modified governing equation was used (Supplementary Note 3).

As another method of theoretical prediction, full 3D multiphysics modelling using COMSOL software (the Solid Mechanics, Electrostatics and Electrical Circuits modules) was used to generate a FEM of the multilayer sensor in greater detail (Methods). Both analytical modelling and FEMs predict the mechanical behaviour and voltage output of the cFaCES accurately (Fig. 2). The accurate prediction of the analytical model[47–52] stems from its accounting of the geometric nonlinearities of the post-buckled beam, indicating that the single-mode model is an accurate approximation of the piezoelectric sensor even in a fully nonlinear testing situation. For example, during certain motions, such as pursed lips (PL), the cheek skin may pucker inwards due to stretching of skin over an internal mouth cavity. For such cases, the strain maps in Fig. 2e are representative, demonstrating that, during stretching on mock skin, some low-amplitude concave buckling occurs, which results in voltage waveforms that are different from that of convex buckling (Fig. 2d).

The extent of nonlinearities that result from axial loading of the sample scale with the amplitude of mechanical excitation. The bare sensor buckles under axial loads of less than ~1 N (Supplementary Fig. 14a and Supplementary Note 4). However, laminating the cFaCES onto a sample of mock skin (thickness, 2 mm) increases the critical buckling load of the system under study and, therefore, changes the voltage response of the cFaCES (Fig. 2d). At low levels of excitation, the beam motion involves an impulse both at the moment of application of the buckling load as well as at its removal but, at larger values of axial deformation, the impulse at the point of force removal disappears. Uniaxial stretching deformations cause notable axial tension in the sample. As a result, the mock skin slides out of the Instron clamping jaws and leads to buckling behaviour in addition to tensile behaviour. To simulate the effects of sliding the specimen out of the jaws, an axial constant force was incorporated into the FEM simulation, an approach based on refs. [48,53]. In post-buckled vibrations of the beams, the effect of axial displacement (Supplementary equation (5) in Supplementary Note 3) is similar to the effect of excitations in the form of an axial force (equation (1)). Identifying the amount of the axial pull out of the specimen by identifying the equivalent axial force in the governing equations therefore enables accurate modelling of mechanical behaviour of the bare cFaCES in the stretching tests (Supplementary Fig. 14b) in a manner that is similar to that for the buckling tests (Supplementary Note 4). Axial force amplitudes for stretching of the cFaCES–mock-skin system are higher than that for the bare sensor. The post-buckled, bi-stable behaviour is therefore clearly visible in the results of this experiment (Fig. 2e). The strain distributions along the cFaCES–mock-skin system for stretching and bending cases are shown in Fig. 2d,e, respectively. Compression forces on the cFaCES and cFaCES–mock-skin system were similarly modelled (Supplementary Note 5 and Supplementary Fig. 16) and confirmed experimentally. These findings establish that the cFaCES is a robust, versatile tool for characterizing mechanical deformations on soft, elastomeric substrates in vitro.

In vivo characterization during facial deformations

Subsequent in vivo study of soft-tissue biokinematics using PG and 3D-DIC completes the system presented herein, as the resultant spatiotemporal strain readings can be used to interpret sensor readings from the cFaCES when laminated onto facial skin during facial deformations. We studied the epidermal strain signatures resulting from 16 different facial deformations, and we compared the effect of these deformations on different regions of the face, such as cheek and temple, as well as the resultant strain and voltage output on the cFaCES when laminated onto those regions.

Initial 3D-DIC tests characterize the properties of the participants' facial skin. An outline of the protocol for in vivo 3D-DIC experiments is provided in the Methods. Experiments were first conducted on the facial skin without the cFaCES laminated, resulting in quantitative measurement of full-field skin strains during various types of natural deformations (Supplementary Videos 2–4). The resulting minimal and maximal principal strain maps for representative motions are shown in Fig. 3a,c,e,g. Strain fields between different participants for the same motion show roughly similar areas of maximum strain, with differences in magnitude or specific spatiotemporal signatures of strain that could be attributed to participant age[18], deviations in motion execution across different individuals and potential muscular atrophy in patients with ALS. All procedures for the tests in the healthy individuals and the patients with ALS were in accordance with the experimental protocol approved by the Committee on the Use of Humans as Experimental Subjects in Massachusetts Institute of Technology (COUHES, no. 1809531633), and the participants gave informed consent.

The results of further 3D-DIC experiments in which a cFaCES was laminated onto human facial skin characterized the behaviour of the cFaCES in vivo (Supplementary Videos 5–7). Laminating the cFaCES onto the skin, as shown in Fig. 3b,d,f,h, decreases the magnitude of the observed strain in the sensor area, which results from the sensor's absorption of the mechanical energy generated by muscle movements that underlie skin deformation. Given that mechanically coupling different materials results in different equilibrium and compatibility constraints in the composite skin–cFaCES system, there results an altered stress–strain distribution

Fig. 3 | In vivo mechanical characterization of the cFaCES on facial skin of healthy individuals and patients with ALS. a–h, Using 3D-DIC, evaluation of facial skin and the top surface of the cFaCES when laminated onto facial skin in vivo characterizes the mechanical interactions between the cFaCES and the facial skin. Analyses for the following two motions are shown: twitch medium magnitude (TM) and eyebrow-down medium magnitude (EDM). **a**,**c**,**e**,**g**, All of the results for skin strain without the sensor on the face (no sensor (NS)). **b**,**d**,**f**,**h**, All of the results for skin strain with the sensor on the face (sensor (S)). **a–d**, Results from a healthy individual. **e–h**, Results from a patient with ALS. The images are strain maps in which strain values, which were calculated using DIC algorithms run on two pairs of cameras, were overlaid onto the raw images captured by PG. The strain maps shown are associated with the frame in which peak strain occurred in the area of the sensor or in the area of the skin directly underneath the location in which the sensor was placed. The strain scale (%) for all of the strain maps is given in the top left corner. The solid boxes indicate the location of the cFaCES; the solid circles indicate its four active elements; and the dashed box indicates the Tegaderm tape. The red circles indicate the sensing element from which voltage data and strain data were collected. For **a–h**, the images on the left and the blue graphs (left, strain, ε (%); right, strain rate $\frac{\partial \varepsilon}{\partial t}$ (percentage per s)) display the results for minimal principal strain; and the images on the right and the red graphs show the same, but for maximal principal strain, as measured on the top surface of the Tegaderm tape layer, which secured the cFaCES to the skin. For each period of 5 s, averaged strain across the DIC-generated triangles ($n \geq 9$), corresponding to the sensing element from which voltage is measured, is represented as a solid line, and the shaded band indicates s.d. The peak strain is denoted in each of the strain graphs by the dashed black line. The black graphs on the right (voltage (top) and voltage rate (bottom)) display the output of the denoted sensing element. Representative strain maps and graphs for all 16 motions are shown for each patient in Supplementary Figs. 17–28. Results of five repeats of the same motion for each individual and each motion are provided in Supplementary Figs. 29–122. Strain maps and graphs include only triangles for which the correlation coefficient was lower than 0.4. The time scale is the same for all of the graphs. Scale bars, 5 cm.

throughout the materials and on the material interfaces. Detailed calculations and explanations of this phenomenon are discussed in Supplementary Note 6. Representative results for healthy individuals and patients with ALS for all motions, with and without cFaCES laminated onto the face, are shown in Supplementary Figs. 17–28. An extensive study on the repeatability of strain field measurements for the same movement and the same participant for testing situations with and without cFaCES lamination is demonstrated in Supplementary Figs. 29–122; small differences in magnitude or strain waveform shape can also be attributed to slight deviations in an individual participant's repeated motion execution over multiple trials.

Modelling of device behaviour during facial deformations

As the piezoelectric elements transform mechanical energy into electrical energy, the observed experimental voltages in 3D-DIC trials can be used to predict the strains expected from the DIC measurements of the top surface deformation of the sensor when laminated onto the skin. Assuming that the cFaCES sensing element area is small enough that the strain is constant over the area of each

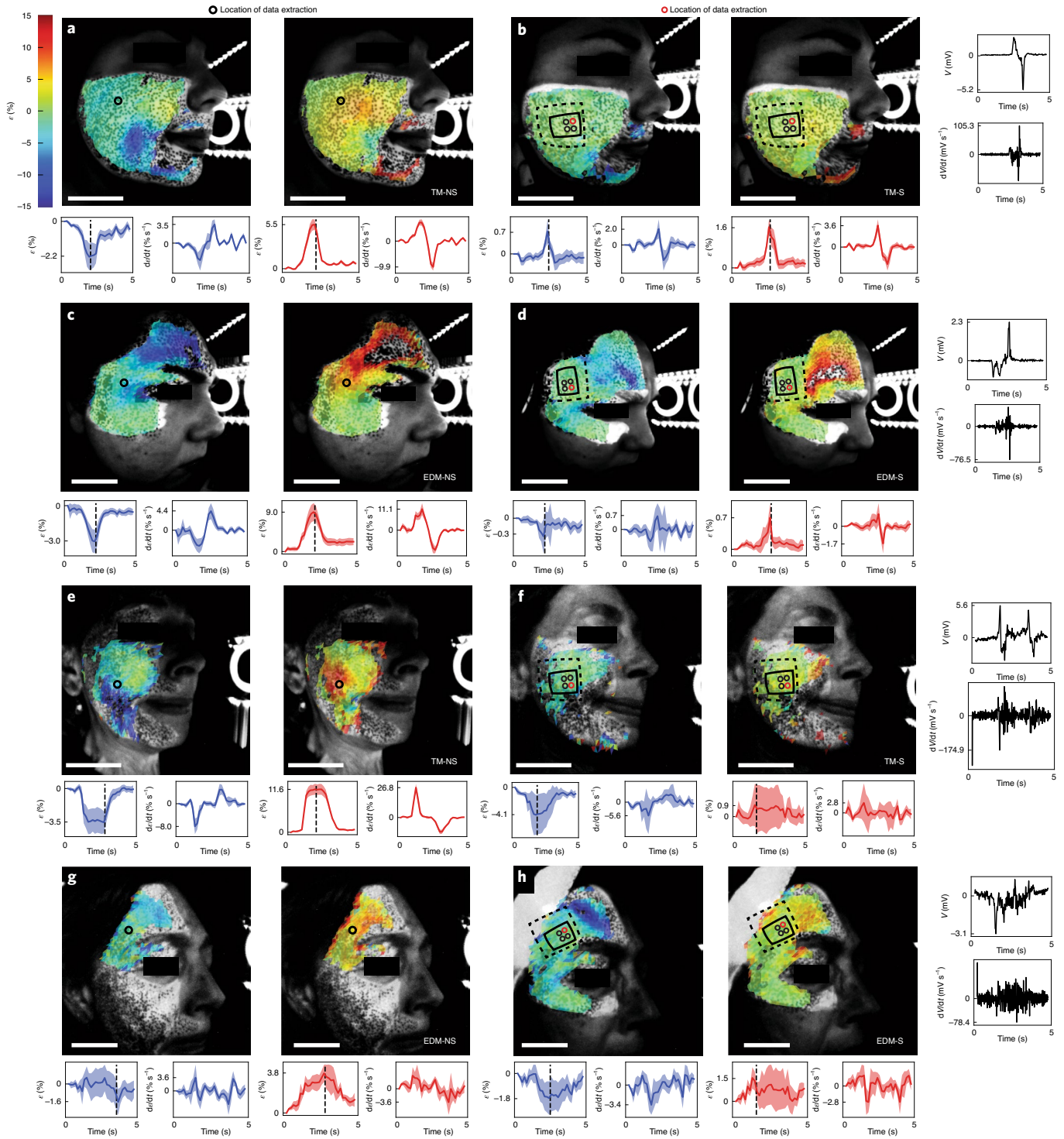

sensor element, we can write the following analytical expression for the sensor voltage:

$$C\frac{dV}{dt}+\frac{V}{R}=e_{31}A\frac{d}{dt}(\epsilon_1+\epsilon_2) \quad (3)$$

where C is the capacitance of the sensor, R is the shunt resistance of the data acquisition (DAQ) system, e_{31} is the effective piezoelectric stress coefficient, A is the area of the piezoelectric element, ε_1 and ε_2 are the strains in the two principal strain directions and $\varepsilon_1+\varepsilon_2$ represents the trace of the eigendecomposed strain tensor where out-of-plane strain, ε_3, is immeasurable and assumed to be negligible for this calculation[58]. The facial gestures do involve shear strains, evident from the appearance of wrinkle lines during some deformations. The buckling showcased by the wrinkles indicates compressive strain normal to the wrinkles and tensile strains along the wrinkles. A combination of compressive and tensile shear strains creates notable shear strains in the non-principal directions. The shear strains are only zero if the coordinate axes are chosen along the strain directions. However, the principal directions could change in time and we therefore derive our equations along a global coordinate system. Shear strains do not affect the generated voltage (equation (3)) as the coupling coefficient between the shear strain in the xy plane and electrical displacement in the z axis is zero. The non-zero coupling coefficient associated with shear deformation is d_{15}, which involves shear deformation along the xz plane and requires electrodes on the lateral surfaces (normal to the x axis).

The voltage output of the cFaCES, which has electrodes in the z direction, correlates with the sum of the planar normal strains, or the surface strain tensor trace (ε_s), which represents the 3D-DIC-measured value of $\varepsilon_1+\varepsilon_2$ from equation (3). To estimate ε_s from the cFaCES-generated voltage, a transfer function was determined. To include all of the sensor layers and improve the accuracy of this model, the full FEM discussed earlier was used instead of the approximate formulas (equations (1) and (2)). For this purpose, we first found the transfer function between the strain on the top surface of the sensor and the output voltage in our FEM. We assumed that the strain is a chirp signal, and ran the FEM to evaluate the voltage output. We then arrived at the transfer function by dividing the Fourier transform of the output by the Fourier transform of the input. The following transfer function is an accurate match for the evaluated transfer function: $\frac{\partial\epsilon}{\partial t}$, where κ is the piezoelectric coupling coefficient evaluated from the FEM simulations. This equation can be further simplified by noting that the skin deformation frequencies are in the order of few Hz, while the resonant frequency of the piezoelectric transfer function is $\frac{\epsilon_1(\omega)+\epsilon_2(\omega)}{V(\omega)}=\frac{Cj\omega+1/R}{\kappa j\omega}$. This simplifies the transfer function to $\frac{\epsilon_1(\omega)+\epsilon_2(\omega)}{V(\omega)}=\frac{1}{Rkj\omega}$. This transfer function is used to predict the strain on the top layer of the cFaCES + Tegaderm tape when the piezoelectric voltage output is known.

The resulting predicted values of strain compared to those that were measured using 3D-DIC are shown in Fig. 4a,b for a few representative motions performed by healthy individuals and patients with ALS, respectively. Measured strains from 3D-DIC show qualitative agreement with strains that were predicted from the cFaCES voltage output for most of the motions for both the healthy individuals and patients with ALS (Supplementary Figs. 123 and 124). Although the exact magnitudes are off due to the simplifying assumptions made in the FEM, the complexity and strain anisotropy of the deformations—that is, surface wrinkling—and limitations on camera and speckling resolution in 3D-DIC (Supplementary Note 6 and Supplementary Fig. 125), the qualitative close match offers an accurate predictive power for strain shape and, therefore, epidermal deformation signature. Asynchronous timing of voltage and strain measurements may result in slight time offsets between experimental observations and theoretical predictions. Results of integrating 3D-DIC-measured strains with cFaCES-measured voltage using theoretical modelling, prediction and validation therefore provide methodologies for establishing predictable and verifiable voltage–strain correlation of cFaCES in vivo. This means that local deformation signatures that result from different facial motions can be predicted on the basis of cFaCES voltage behaviour, setting the stage for explorations with RTD.

Furthermore, 3D-DIC results without the sensor can be used to determine a sensor placement location such that the four piezoelectric elements of the cFaCES experience computationally distinguishable epidermal deformation signatures—that is, spatiotemporal strain profiles—during distinct motions for an individual. This is useful for RTD, in which the sensor should be placed such that each motion can be uniquely identified by the measured voltages in each sensing element. Given that the sensor remains laminated onto the same location during the occurrence of different facial motions, the goal is to maximally differentiate the voltage waveforms generated by the four cFaCES piezoelectric elements.

Most biomedical sensor designs lack an in-depth study of the target soft tissue before the design and fabrication of the sensor that is meant to couple to that tissue. Here, we propose that 3D-DIC can be used as a method for in-depth biokinematic study of the target region on which a sensor with mechanically active functional material, such as piezoelectrics, will be placed. Similar to how chemical assays of a body part would be conducted before designing medication for disorders of that body part, 3D-DIC also enables the mechanical study of biological soft tissue before designing the mechanically active functional materials on mechanically adaptive substrates that are meant to intimately integrate with that soft tissue. We specifically used 3D-DIC results to determine the validity of the size and spacing of AlN piezoelectric elements (see the 'Device design considerations' section in the Methods). Indeed, given the above discussion demonstrating sensor voltage correlation with ε_s (Fig. 4), contour maps (with isolines measured using ε_s) can be

Fig. 4 | 3D-DIC and theoretical modelling for prediction and validation of cFaCES performance in vivo. a,**b**, Experimental (Exp) surface strain tensor trace (ε_s) (blue) and cFaCES voltage (black) data were simultaneously collected and recorded while the participant performed various facial motions, and were analysed to determine the validity of measured strains and the capability of the theoretical model to predict surface (top of Tegaderm tape layer) strain given the sensor voltage output. Analyses for the following four motions are shown: smile medium magnitude (SM), twitch medium magnitude (TM), eyebrow-down medium magnitude (EDM) and pursed lips (PL). The '-S' for each motion label indicates that all of the results are for the strain with the sensor laminated on the face. For each period of 5 s, averaged ε_s across the triangles ($n \geq 9$) generated by DIC corresponding to the sensing element from which voltage is measured is represented as a solid line, and the shaded band indicates the s.d. The peak strain is denoted in each of the strain graphs by the dashed black line. Voltage graphs (black) display the output of the denoted sensing element (red circle). Theoretical (Th) prediction (orange) of in vivo with ε_s from the voltage output of a cFaCES when laminated on facial skin was qualitatively and quantitatively similar to the experimentally observed strains from 3D-DIC under the same conditions for the healthy individual, but deviated for the patient with ALS. The images show spatiotemporal ε_s maps in which strains that were calculated by DIC algorithms run on two pairs of cameras were overlaid onto the raw images captured by PG. The strain maps shown come from the frame in which peak strain occurred in the area of the sensor. The strain scale bar (%; top left) applies to all of the strain maps in **a** and **b**. For all strain maps from DIC trials with the sensor, the solid boxes indicate the location of cFaCES; the solid circles indicate its four active elements; and the dashed boxes indicate the Tegaderm tape. The red circles indicate the sensing element from which voltage data and strain data were collected. The results shown are from a healthy individual (**a**) and a patient with ALS (**b**). The time scale is the same for all graphs.

generated from 3D-DIC results and used to determine sensor design parameters and sensor placement location. For determining sensor placement location, these contour maps for different motions were made translucent (50%) and were overlaid on top of each other (this process was repeated over three time points during the facial deformation) to determine, by inspection, an area of facial skin where the

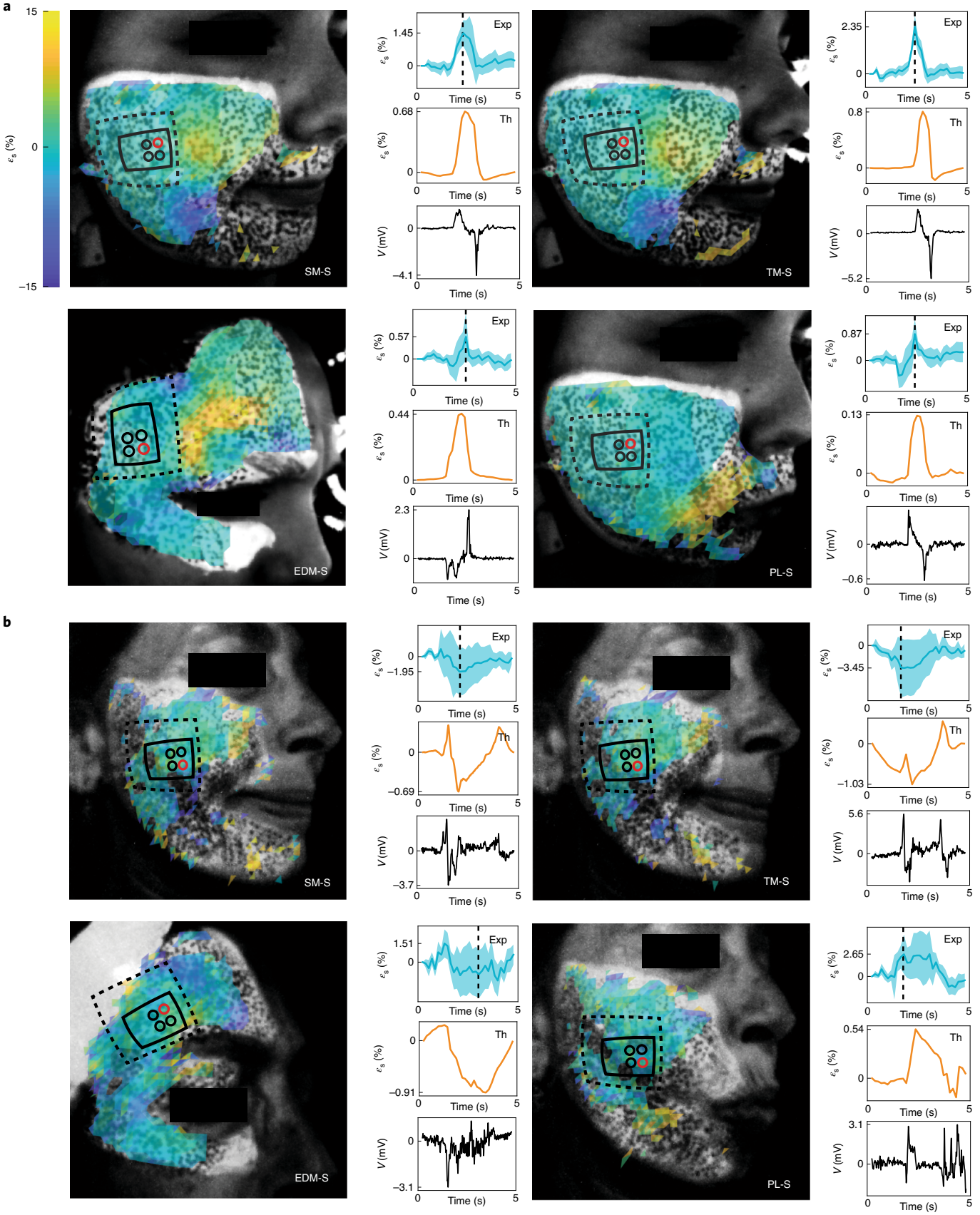

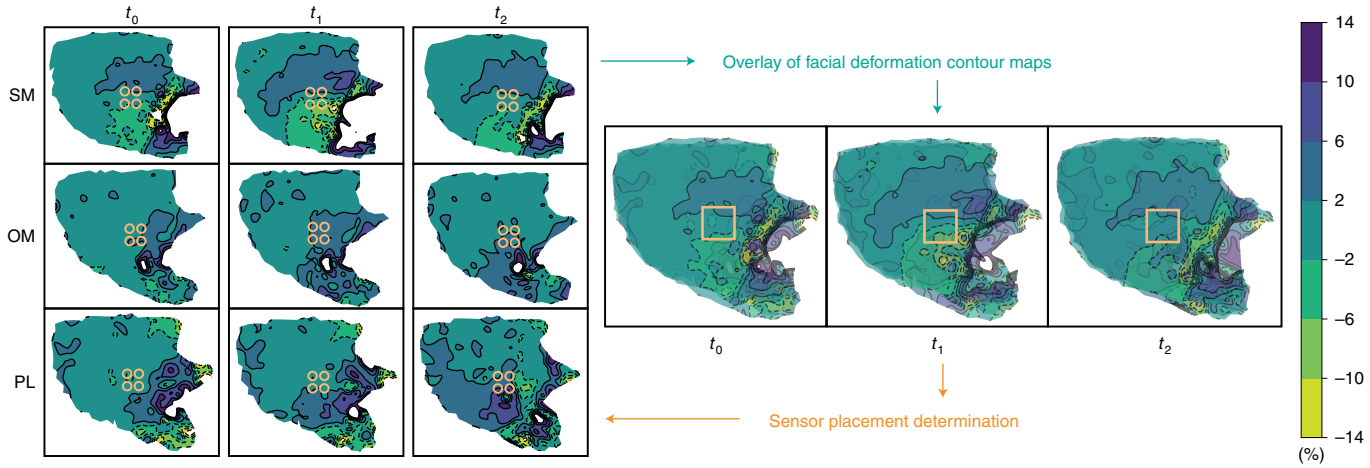

Fig. 5 | Sensor placement for RTD informed by analysis of skin strains from 3D-DIC. Contour maps generated from skin strains without a cFaCES laminated onto the skin help to guide the placement of cFaCES onto facial skin such that the strain observed by each of the four sensing elements is temporally distinct for different motions. Overlaying contour maps from similar motions observed at the peak strain enables qualitative selection of sensor placement. The orange square indicates a potential location for the four sensing elements that would result in distinct strain observations on each element.

four cFaCES piezoelectric elements would experience distinct spatiotemporal strain signatures (Fig. 5), which could purportedly lead to computationally distinguishable voltage waveform signatures. Future automation of determining a sensor placement location by code written to analyse the spatiotemporal strain contours would be possible using machine vision algorithms.

RTD and classification of facial deformations

When laminated onto the facial skin, the low-cost, mass-manufacturable cFaCES enables the creation of a library of motions from which a large subset of human language could possibly be inferred. The size of this subset depends on the method of mapping facial motions to language as well as the number of distinct facial motions that are chosen for decoding. The final number of motions chosen for decoding will depend on the number of phrases or ideas that are desired to be communicated as well as the chosen mapping strategy. As an example, Fig. 6a shows how different strategies for this mapping—that is, direct, tree and conditional—affect the total number of possible ideas or actions that the user can communicate using seven motions. The motion library can be created by each user, on the basis of their preferences and comfort. Each motion can be classified as one of the motions in the library by a RTD algorithm, which uses a dynamic-time warping, *k*-nearest neighbours (*k*NN–DTW) model[59–61], as shown in Fig. 6a. The *k*NN–DTW algorithm predicts the most probable motion on the basis of calculating the distance between each of the voltage waveforms detected during testing with all of the detected waveforms in the training set for the model. Motion classification relies on calculating the distance between sets of voltage waveforms from two motions. It is important to note that the *k*NN–DTW algorithm effectively compares the voltage waveform shapes rather than voltage values or principal-component analysis. For each detected motion, n voltage waveforms are captured, each one corresponding to a particular sensing element on cFaCES. Distances d_i between the voltage waveforms corresponding to the same element i are calculated, and the r.m.s. value is then calculated to obtain the total distance $d = \sqrt{\sum_{i=1}^{n} (d_i)^2}$ between an observed signal and a signal in the training set, where n is the total number of sensing elements. Each distance d_i is calculated from DTW and, specifically, an approximation for DTW, which coarsens the temporal resolution of the voltage waveform, computes a warped distance matrix between two signals at that lower resolution, and projects that matrix back into finer resolution. This algorithm has previously been developed and built into a Python library called fastdtw[62], which was adapted for use in this *k*NN–DTW model. Once the total distance between the detected motion and each of the motions in the training set is calculated, the *k*NNs—that is, the voltage waveform sets with the k lowest total distances—are identified and their motion labels are used to determine the weighted-average probabilities of each motion label. The motion with the highest probability is labelled the 'classification' of the detected motion.

In the RTD system, the cFaCES is laminated onto the facial skin and connected to a custom-built signal-processing board (SPB) that performs differential voltage amplification, analogue signal filtering and analogue-to-digital conversion (Supplementary Fig. 126), and the output of which is connected to a Raspberry Pi for portable application. The onboard processor of the Raspberry Pi runs the *k*NN–DTW algorithm code files, which were written in the Python language (v3.6). Before RTD can be tested, the participant completes a training session that involves performing a motion 12 times. Each motion is identified in the code, and the interval of 4 s containing the motion-induced voltage output (100 Hz sampling rate) of the sensor is detected, stored and filtered digitally using a sixth-order low-pass Butterworth filter with a 6 Hz cut-off frequency. This is repeated for each distinct motion type in the participant's desired library, and forms the calibration set. The participant then performs a series of motions that are classified in real-time using the *k*NN–DTW algorithm (Supplementary Video 8). The extent of the 'real-time' aspect of our decoding algorithm is qualified by the average lag time (mean ± s.d.) between the end of the user's performance of the motion and the display of the classification result, which is 1.71 ± 0.12 s (Supplementary Table 3). Evaluation of the RTD system on healthy individuals and patients with ALS involved measuring the testing accuracy, and is shown in Fig. 6b,c, respectively. Eight voltage waveforms were randomly selected from each motion in the calibration set, forming the training set. Testing accuracy refers to the percentage of motions that were correctly identified from the remaining four voltage waveforms from each motion in the calibration set when predicted using a model containing the training set. The testing accuracies reported here were calculated after evaluating the RTD model using threefold-stratified cross-validation, resulting in 27 different dataset combinations for each combination of piezoelectric elements usable for model evaluation.

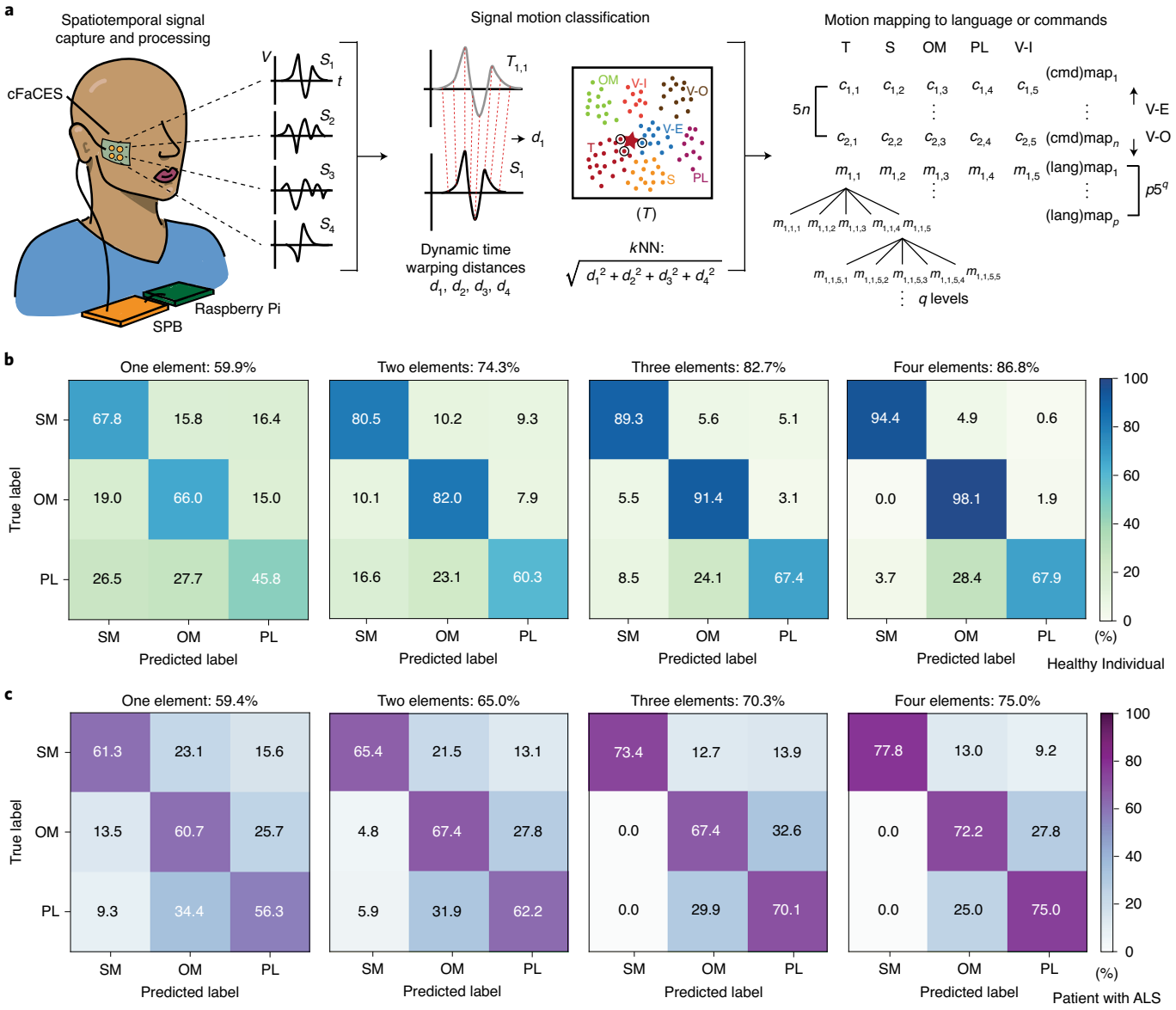

Fig. 6 | RTD of facial motions and library construction. a, Schematic of the RTD system. A cFaCES is laminated onto the face and its four sensing elements $i = \{1,2,3,4\}$ are connected to a SPB for differential signal amplification and analogue-to-digital conversion. The voltage waveforms from each of the four cFaCES sensing elements are indicated by S_i. The digital signal from the SPB is fed to the Raspberry Pi, which automatically detects facial motions and classifies them as one of the motions in the individual's library of motions. The classification is based on a *k*NN–DTW algorithm, modified to calculate the $k = 3$ nearest neighbours on the basis of the magnitude of efficiently calculated dynamically time warped distances d_i of the signals of each of the four sensing elements, with total distance calculated as $d = \sqrt{\sum_{i=1}^{n} (d_i)^2}$. $T_{i,j}$ represents the *j*th signal from sensing element *i* in the training data. The classified motion can be used to create a library of any desired size, due to the potential to assign either additive, multiplicative or exponential meaning to each motion. In the example mapping on the far right of **a**, seven motions are used: twitch (T), smile (S), open mouth (OM), pursed lips (PL), mouthing the vowel 'I' (V-I), mouthing the vowel 'E' (V-E) and mouthing the vowel 'O' (V-O). In this mapping, five selector motions (T, S, OM, PL and V-I) are used to select options within each command or language message menu, indicated by (cmd)map and (lang)map, respectively. Two scroll motions (V-E and V-O) are used to scroll through *n* different command sets in a multiplicative map in which there are $5n$ total selectable commands (*c*). These motions can also scroll through *p* language sets, and the five selector motions can then navigate through message options arranged in a tree-like exponential mapping with *q* levels, leading to $p5^q$ total selectable messages (*m*). **b**,**c**, Threefold-stratified cross-validation for model evaluation results in average testing accuracies of the RTD system for a healthy individual (**b**) and a patient with ALS (**c**). The average (mean ± s.d.) of overall classification accuracies involving only one element was 59.9 ± 2.1% ($n = 675$) and 59.4 ± 4.7% ($n = 135$) for the healthy individual and the patient with ALS, respectively. For two elements, the accuracies were 74.3 ± 1.4% ($n = 783$) and 65.0 ± 7.9% ($n = 27$) for the healthy individual and the patient with ALS, respectively. For three elements, the accuracies were 82.7 ± 1.8% ($n = 405$) and 70.3 ± 10% ($n = 27$) for the healthy individual and the patient with ALS, respectively. For four elements, the accuracies were 86.8 ± 3.0% ($n = 324$) and 75.0 ± 17.4% ($n = 27$) for the healthy individual and the patient with ALS, respectively. As the number of sensing elements used in RTD is increased, the accuracy of motion classification increases.

Here, we show the results of RTD that was performed using a small subset of three motions (smile medium (SM), open mouth (OM) and PL) by healthy individuals and patients with ALS, with a focus on testing the effect on the testing accuracy of increasing the number of piezoelectric elements n used for classification. For a given sensor for which n elements are usable for RTD, evaluation was performed for every combination of $j \leq n$ elements. RTD evaluation suggests that increasing the number of elements improves the testing accuracy, as shown in Fig. 6b,c. The average (mean ± s.d.) of overall classification testing accuracies involving only one element was 59.9 ± 2.1% and 59.4 ± 4.7% for the healthy individual and the patient with ALS, respectively. For two elements, the accuracies were 74.3 ± 1.4% and 65.0 ± 7.9% for the healthy individual and the patient with ALS, respectively. For three elements, the accuracies were 82.7 ± 1.8% and 70.3 ± 10% for the healthy individual and the patient with ALS, respectively. For four elements, the accuracies were 86.8 ± 3.0% and 75.0 ± 17.4% for the healthy individual and the patient with ALS, respectively. Examples of voltage signals that were simultaneously recorded from all four elements of a cFaCES laminated onto the cheek are shown in Supplementary Fig. 127. This observation suggests that it is important to use multiple spatiotemporal signals—that is, multiple sensing elements—to improve the accuracy of RTD. The cFaCES design allows for a maximum of four such sensing elements, but further increasing the number of elements used for RTD could potentially make decoding accuracy even higher. However, it is possible that certain motions may be too similar for a given individual, for example, the case of OM and PL for a healthy participant (Fig. 6b) and, for such cases, only one of those motions should be included in the individual's nonverbal communication library to increase decoding effectiveness.

To evaluate the potential for the RTD system to be used across a wider range of motions, we studied the classification testing accuracy of the kNN–DTW algorithm, again using stratified cross-validation, on a set of post-recorded cFaCES single-element signals (Supplementary Fig. 128). For four, six and eight motions, the accuracies were 89.3 ± 18.5%, 65.5 ± 16.6% and 50.1 ± 23.9%, respectively. Given these positive results from single-element signals, and the clear potential for improvement of the accuracy with increasing number of elements included in RTD (Fig. 6b,c), it is viable to use the RTD system reported here for a wider range of motions in future studies. Although our study aims to achieve a balance between real-time computational load and decoding accuracy, a further easily achievable increase in testing accuracy could result from increasing the number of voltage waveforms per motion collected in the calibration set and used in the training set[63,64]. For this representative study, we establish the potential for the cFaCES to be used as part of a nonverbal communication interface.

Outlook

The concepts, materials, system design and characterization methods introduced here offer new routes for rapid in vivo biokinematic assessment of epidermal surfaces during dynamic movements. The conformable nature of the sensors, together with their predictable responses that are consistent with theoretical models, offer a high-performance operation that is cross-validated with 3D-DIC studies. Non-contact, full-field optical strain assessment methodologies coupled with theoretical models have wide applicability for design, placement and cross-validation of a host of conformable on-body sensors[27,28], even when they are laminated onto highly curvilinear regions of the body. Particularly, 3D-DIC studies coupled with detailed 3D multiphysics simulations and analytical calculations have the potential to characterize in vivo strain sensing by modalities other than piezoelectric elements and even inform mechanically adaptive device design. In vivo RTD trials of facial motions to evaluate the proposed fully characterized device for use as a nonverbal communication interface demonstrated that increasing the number of sensing elements used in classification led to increased testing accuracies. The present limitations of the cFaCES system are as follows: (1) low density of sensing elements, (2) small area coverage, (3) wired connections and (4) external adhesion mechanism (Tegaderm tape). Specifically, low spatial resolution and small area coverage of the sensing elements, although ensuring low computational load, nevertheless limit the ultimate distinguishability of a large set of distinct facial motions ($n > 8$). Future embodiments might incorporate high-density, further-miniaturized arrays of sensing elements to increase spatial coverage and, therefore, improve language classification accuracy across a wide variety of motions, which could greatly increase the library size of facial motions. Scaling the spatial density of strain measurements attainable by the cFaCES from its present form (2 × 2) to a larger configuration ($n \times n$) would necessitate careful routing of a larger number of interconnects, further streamlined fabrication flow and improvements in the signal processing circuitry (that is, by implementing multiplexing). As our system serves to project the capabilities of a first-prototype low cost, computationally light, conformable nonverbal communication technology, wireless data or power transmission components were not pursued in this study. However, such systems may be developed to co-integrate with wireless communication for continuous clinical monitoring of a wide range of neuromuscular conditions, in which variations of strain values measured by cFaCES are anticipated due to either time-dependent alterations in muscle movements and, therefore, measurable epidermal deformations due to neurodegeneration, or a response throughout medical therapy.

Methods

Device design considerations of a cFaCES. AlN was used as the piezoelectric material in cFaCES for several reasons: its low cost[65], complementary metal oxide semiconductor (CMOS)-compatible processing[34,35] and its lead-free nature, making the material more suitable for mass manufacturing, clinical translation and adoption in future lead-free industrial standards[36,37]. From a processing standpoint, piezoelectric AlN thin films are usually prepared using a reactive sputtering process in N_2–Ar plasma, with an Al target. Here, the reactive sputtering process is compatible with the standard 200-mm wafer process, making it suitable for mass production[66]. The CMOS-compatible nature of the AlN piezoelectric layer further enables ease of mass manufacturability. Although AlN has lower piezoelectric coefficients than standard thin film piezoelectrics such as PZT[25], PZT is not CMOS-compatible and may be subject to aging and other material property changes over time[67]. As a post-CMOS-compatible piezoelectric material, AlN-sputtered thin films are commercially used in fingerprint sensors[68] and thin-film bulk-wave acoustic resonator filters[69,70]. Owing to its low-cost microfabrication and mass-production capability using microelectromechanical systems (MEMS) technology, AlN-based resonators have been developed that have been proven to operate above 6 GHz for 5G mobile communication[71]. Finally, the kNN–DTW RTD algorithm used here classifies facial motions on the basis of piezoelectric voltage waveform shapes rather than voltage values (Supplementary Fig. 127); the relatively lower voltages generated by AlN piezoelectrics are therefore not an issue in our nonverbal communication technology.

Furthermore, functional AlN thin films have been demonstrated widely on flexible substrates (usually polyimide or polyethylene terephthalate)[32,72–76]; however, the use of AlN thin films in conformable, stretchable conditions has not yet been demonstrated owing to difficulties in the microfabrication processing techniques. Conventionally, high-quality AlN thin films are manufactured on Si wafers with or without a layer of SiO_2 and, therefore, most AlN MEMS devices are rigid[77–79]. Here we present microfabrication techniques that maintain the CMOS-compatible, low-cost nature of AlN in a conformable form factor for coupling with the highly curvilinear surfaces of the face (Fig. 1) while remaining operational during high-strain, cyclic dynamic stretching and buckling deformations that are involved in facial motions on the cheek and temple (Figs. 2 and 3). The full width at half maximum (FWHM) of X-ray diffractometer (XRD) rocking curve is one well-established criteria for determining the quality of the synthesized AlN along the c-axis. Supplementary Table 2 compares the FWHM of this research with other studies of AlN thin films on rigid and flexible substrates. Although AlN has been reported to be fabricated on polymeric substrates, such as polyimide and parylene, their FWHM of XRD rocking curve are substantially higher than that of AlN on Si or SiO_2, as a consequence of the rough surface of the polymeric substrates and large lattice strain mismatch. Here we developed a new microfabrication process to enable the flexible AlN sensor without undermining the quality of the AlN crystal thin film. The FWHM of the AlN in this study is only 1.69° (Supplementary Fig.

5 and Supplementary Table 2), fairly close to those on Si-based substrates. Thus, our microfabrication process of AlN maintains cFaCES as a conformable device without sacrificing functionality.

The thickness of the AlN piezoelectric layer was chosen by considering the trade-off between the signal-to-noise ratio (SNR) and the bendability of the final device that comes with changing the thickness of AlN. A thicker (thinner) AlN layer results in higher (lower) SNR, due to higher d_{33} coefficient[80], and reduced (greater) bendability. Theoretical modelling results show that increasing the thickness of the AlN layer increases the voltage output of the cFaCES, but decreases the minimum allowable ROC before fracture (Supplementary Note 2 and Supplementary Fig. 129). As the *k*NN–DTW algorithm distinguishes between distinct motions by voltage waveform shape instead of value, the exact thickness of the AlN layer would negligibly affect the detection accuracy, provided that the signal processing circuitry can reliably filter and amplify the voltage signal generated by this piezoelectric layer. Finally, from a processing standpoint, when growing a thicker AlN layer, more defects appear and the *c*-axis orientation of AlN is gradually undermined[81]. The non-*c*-axis oriented AlN has negative effects on its piezoelectric properties. In this study, the 1.5-μm-thick AlN has been proved to be highly *c*-axis oriented by TEM and XRD rocking curve (Supplementary Fig. 5).

Mo was selected as the electrode material due to the reduced lattice mismatch that it provides for the piezoelectric layer, as well as its compatibility with the MEMS process. To ensure the high quality of the *c*-axis texture of the AlN layer, a critical strategy is to reduce lattice mismatch between the underlying metal layer and the AlN layer. The lattice parameter of AlN ranges from 4.978 Å to 4.982 Å for the *c*-axis. Despite the fact that high-quality AlN has been synthesized on Mo (110), Al (111), Pt (111), Ti (002) and Au (111) substrates due to their reduced lattice mismatch, a large concentration of nitrogen was reported to incorporate into Ti and Al layers, which undermines the electrode conductivity (nitrogen plasma reacts with Al to form AlN during the reactive sputtering process)[34,82–84]. Moreover, Pt, Au and Ag are not CMOS-compatible materials, and they cannot be etched by dry-etching processes using MEMS technology. By contrast, Mo is a CMOS-compatible material that can be precisely etched by the mixture of O_2/Cl_2/Ar inductively coupled plasma. A Mo bottom layer also provides good adhesion for the AlN layer[85]. Finally, conductive materials for the cFaCES were selected such that relatively low-cost, widely available materials that are often used in current manufacturing or microfabrication processes can be used. Although conventional electrode materials used in research, such as Au, Pt and Ag, could have been used for greater ductility, Mo electrodes and Al bonding pads were used for their relatively low cost and standard usage in industrial processes[86–88]. The limited thickness (200 nm) and serpentine structures of the Mo electrodes enable increased stretchability despite lower ductility compared with precious metals[89].

SiO_2 was chosen as the encapsulation material due to a few processing concerns. The growth of SiO_2 on the Si test wafer can better ensure a flat surface, in terms of surface roughness, compared with using other polymer materials. The flat substrate surface enables the growth of highly crystalline AlN along the *c*-axis[90]. The use of SiO_2 as the substrate layer for AlN growth during microfabrication is the primary reason why the AlN layer in cFaCES has a similar piezoelectric effect to those grown on rigid silicon, as evidenced by the XRD rocking curve (Supplementary Fig. 5). Furthermore, SiO_2 is a dielectric material that is commonly used for the insulation of MEMS devices, so it is a well-known, relatively inexpensive material in standard cleanroom procedures. Furthermore, the plane-strain modulus (Supplementary Note 2) of SiO_2 is 25 times greater than that of polyimide. Thus, roughly the same NMP of cFaCES can be achieved with a thinner layer of SiO_2 compared with polyimide, which allows for less material usage.

We used our developed theoretical models to study the effects of the design parameters (thicknesses, sizes, shapes and distances in-between elements) on the performance of a cFaCES. Two types of models were developed for this purpose. The first is the FEM, which can include all of the intricate details and complexities of the cFaCES. The second are analytical models that rely on effective simplifications of the sensor and give closed-form relationships that better reveal the design decisions. There are two key design objectives studied using these models. The first objective is voltage sensitivity (that is, the amplitude of the generated voltage for a given facial strain). Larger voltage sensitivities enhance the SNR and are therefore preferable. The second objective is the compliance of the cFaCES sensor. If the sensor is notably stiffer than the skin, it will notably affect the skin deformations, potentially diminishing the amplitudes of those deformations. This not only will be uncomfortable for users, but also will make the cFaCES dysfunctional. Detailed results from the theoretical models of this study reveal that, the thicker the AlN layer, the greater the voltage sensitivity and the lower the sensor compliance. The cFaCES has enough voltage sensitivity to respond to facial deformations (~0.5–15%; Supplementary Figs. 29–122) and, at the same time, does not disrupt the facial motions. Although increasing the AlN thickness improves the voltage sensitivity, it does not notably increase the accuracy of the device, as the current dimensions result in high SNR for all cases. However, increasing the AlN thickness will make the cFaCES more rigid than the skin and will disrupt facial motion. The present dimensions are therefore close to the optimal values for our multiobjective optimization problem.

Our main method for parametric study is FEM, which can handle all of the details and complications of the cFaCES sensor, including all layers. We studied the effect of the design parameters on (1) the generated voltage (that is, the sensitivity of the cFaCES) and (2) the stiffness of the cFaCES (that is, the feel of the sensor).

In the sensitivity analysis, we examined the voltage generation of the sensor when subjected to a sinusoidal uniaxial facial strain of 1% amplitude. As shown in Supplementary Fig. 129a, the amplitude of the generated voltage increases with the thickness of the sensing elements and decreases with the thickness of the substrate PDMS layer. This suggests that, the thicker the AlN layer, the greater the voltage sensitivity, and the only limitations for the AlN thickness are set by fabrication. However, this verdict is contradicted by the fact that, if the AlN layer is thick, the cFaCES will be too stiff—it will not only feel uncomfortable, but it will also diminish facial gestures (the very thing it should measure).

To analyse the stiffness (and the feel) of the sensor, we calculated the axial stiffness from the equation $k = \frac{F_x}{\delta_x}$, where F_x is the force applied to one end of the sensor in *X* direction and δ_x is the displacement in the *X* direction. In this analysis, we applied forces at the two ends of the cFaCES and simulated its deformation using COMSOL. We measured the motion of the two end faces and used it in the aforementioned formula. As shown in Supplementary Fig. 129b, increasing the AlN thickness increases the overall stiffness of the cFaCES.

The critical stiffness value for the cFaCES is the skin stiffness. We compared the stiffness of the cFaCES to the stiffness of the skin. If the stiffness of the sensor is notably larger than the skin stiffness, it will affect the skin motion. The stiffness of the skin is estimated as $k = \frac{E_s}{\delta_x}$, where E is Young's Modulus, A is lateral area and L is length of skin under the sensor. The Young's Modulus of the skin is assumed to be $E \approx 31$ kPa (ref. [91]) and thickness ~6.39 mm (this corresponds to experimental average values from cheek skin)[92]. The resulting estimated value of the stiffness of the skin is 113 N m^{-1}. The present device design with 1.5-μm-thick AlN has a stiffness of 166 N m^{-1}, which shows that the stiffness of the device is close to the skin stiffness; therefore, cFaCES does not fundamentally change the skin stiffness.

The cFaCES piezoelectric elements themselves are much stiffer than the cFaCES substrate material and human skin; therefore, changing the size (lateral area in the *xy* plane) of the piezoelectric elements affects the cFaCES stiffness considerably. The chosen lateral area was determined by evaluating the trade-off between (1) large size diminishing spatial resolution of strain measurement while increasing the stiffness, and (2) small size resulting in low voltage sensitivity (Supplementary Fig. 129c). The chosen value of lateral area was ~0.725 cm^2, resulting from an AlN element radius of 0.24 cm.

However, the shape of piezoelectric elements does not affect the cFaCES stiffness provided that the lateral area and thickness remain constant, which means that a cFaCES with square piezoelectric elements of side length $k = \frac{EA}{L}$ results in the same cFaCES stiffness as a cFaCES with circular piezoelectric elements of radius *r*. We performed two FEM models with the same piezoelectric lateral area. One has circular patches with a radius of ~0.24 cm and the other has rectangular patches with a side length of ~0.42 cm. The sensor was pulled with a specific force from one side and the average displacement field of that side in the same direction was measured. As shown in Supplementary Fig. 129d, both models have the same displacement field distribution, which confirms that sensor stiffness is independent of the shape.

We further developed an analytical model to show the relationship between the output voltage and the amount of shear force exerted to the device. The electric displacement vector $\mathbf{D}$ can be defined as $\mathbf{D} = \frac{Q}{A_p} = d_{31}\sigma_{xx} + \varepsilon\mathbf{E}$ (ref. [93]), where Q is the electric charge, A_p is the lateral area of piezoelectric element, ε is the dielectric constant matrix, $\mathbf{E}$ is the electric field vector, d_{31} is the piezoelectric coefficient and σ_{xx} is the *xx* component of the stress matrix. As there is no external voltage applied to the piezoelectric patch, the equation reduces to $\mathbf{D} = d_{31}\sigma_{xx}$. The electric charge is therefore $Q = d_{31}\sigma_{xx}A_z$, where A_z is the lateral area of the electrode. Furthermore, for a simple beam comprising a piezo layer and a substrate layer, the tension in the longitudinal direction is given by $F_{xx} = \frac{k_p}{k_p+k_s}F$, where F_{xx} is the force in piezo layer, F is the total force applied to the beam, and k_p and k_s are stiffnesses of the piezo and substrate, respectively, which can be calculated by $F_{xx} = \frac{k_p}{k_p+k_s}F$ and $k_p = \frac{E_p t_p w}{L}$ (ref. [93]; where p and s subscripts refer to piezo and substrate layers, E is Young's Modulus, t is the thickness of layer, w is the width of the sensor and L is the length). Thus, the tension can be written as $\sigma_{xx} = \frac{k_p}{k_p+k_s}\frac{F}{t_p w}$. On the basis of this, the electric charge can be rewritten as $Q = d_{31}\,Lw\frac{k_p}{k_p+k_s}\frac{F}{t_p w}$. One can solve for the instantaneous current in the circuit by taking the time derivative of both sides and writing Kirchhoff's law for the current, which yields $Q = d_{31}\,Lw\frac{k_p}{k_p+k_s}\frac{\dot{F}}{t_p w}$, where $\alpha = \frac{d_{31}\,LE_p}{E_p t_p + E_s t_s}$, C is the capacitance of the simplified sensor model, V is the voltage generated, R is the equivalent resistance and $\dot{\alpha} = \frac{d_{31}\,LE_p}{E_p t_p + E_s t_s}$ is the time derivative of the applied force. Furthermore, one can form the transfer function between the voltage as output and force as input and rearrange terms in the following format $\frac{V(s)}{F(s)} = \frac{\alpha s}{Cs+\frac{1}{R}}$. The frequency response function of the above transfer function is shown in Supplementary Fig. 128e.

Similarly, for the case of constant strain, one can formulate the electric-charge density as $\frac{V(s)}{F(s)} = \frac{\alpha s}{Cs+\frac{1}{R}}$, where e is the stress piezoelectric matrix, ε_{xx} is the strain component *xx*, ε is the dielectric matrix with the coefficients of electric permittivity on its diagonal and $\mathbf{E}$ is the electric field vector. The external voltage applied is zero and so is the electric field E; therefore, $D = e_{31}\varepsilon_{xx}$. The electric charge

along the electrodes are therefore obtained by $Q = e_{31}\varepsilon_{xx}A_z = e_{31}\varepsilon_{xx}Lw$. Taking the time derivative of both sides of the equation and using Kirchhoff's Law yields to $D = \frac{Q}{A_p} = e_{31}\varepsilon_{xx} + \varepsilon\mathbf{E}$, where $\beta = e_{31}Lw$. Taking the Laplace transform of both sides of the equation and rearranging the terms with respect to voltage leads to $\frac{V(s)}{\varepsilon_{xx}(s)} = \frac{\beta s}{Cs+\frac{1}{R}}$, which describes the transfer function between the voltage and strain for the case in which the strain is assumed to remain constant. The frequency response function of this transfer function is provided in Supplementary Fig. 128f.

The total force exerted on the device can be obtained using the equivalent stiffness k_{eq}, which relates to the force F by $F = k_{eq}\delta$ (ref. [94]), where δ is the uniaxial displacement. The strain can therefore be calculated by $\frac{V(s)}{\varepsilon_{xx}(s)} = \frac{\beta s}{Cs+\frac{1}{R}}$. Similarly, the total stress in the device section can be obtained by $\varepsilon = \frac{\delta}{L} = \frac{F}{k_{eq}L} = \frac{F}{w(t_pE_p+t_sE_s)}$. We can define the equivalent modulus of elasticity for the device by $E_{eq} = \frac{\sigma}{\varepsilon} = \frac{t_pE_p+t_sE_s}{t_p+t_s}$ (ref. [94]). From this equation, it is clear that the equivalent stiffness and elastic modulus of a cFaCES are more sensitive to the variation of the piezoelectric layer thickness compared with that of the substrate, because the elastic modulus of the piezoelectric layer is two orders of magnitude higher than that of the substrate.

From a user-experience standpoint, we considered the effect of the size of the entire device. A large device area (that is, covering nearly the whole face) may be quite uncomfortable for continuous lamination onto the skin of patients with ALS. Furthermore, a large-area sensor would involve more unnecessary signals, rendering the RTD much more complex. With such considerations, we felt that a 2.5 cm × 3.5 cm device with a ~1.1 cm × 1.1 cm sensor array, which can cover the areas in which dynamic deformations of the skin occur during facial motions (Fig. 5), could provide functionality without diminishing user comfort too greatly.

Finally, the strategy for determining the size and spacing of the sensing elements directly relates to the strain contour maps given in Fig. 5. In addition to the voltage generation (Supplementary Fig. 129c) and stiffness considerations discussed above, we evaluated contour maps generated by 3D-DIC (see the 'Modelling of device behaviour during facial deformations' section in the main text) to determine whether the radius of the AlN piezoelectric element is sufficient to capture the dynamic strain deformation patterns occurring on the face during facial motions. An element that is too large would average out and, therefore, lose the spatiotemporal dynamics of the facial deformation strains, whereas an element that is too small would require too large of an array, resulting in a high computational load for the RTD classification algorithm. On the basis of a study of 3D-DIC contour maps, the minimum spacings between strain isolines (each representing a 3% gradation change) for various motions ranges from 0.15 cm to 0.27 cm in the target region of interest for the sensor (Supplementary Fig. 130). The choice of an element radius of 0.24 cm (and, therefore, a diameter of 0.48 cm) would provide an acceptable choice by which ~3% strain gradations can be appropriately deduced by the piezoelectric elements without too much loss of dynamic strain data and without requiring too large of an array of elements. Given the size of the piezoelectric elements and the desired size of the element array (2 × 2), it is important to note that the one-time data gathered by 3D-DIC can be used as a method to determine where sensing elements can be located to maximize distinguishability. For our study, we designed the spacing to strike a balance between two factors: (1) to be able to distinguish between the local strain deformation patterns, as identified by 3D-DIC contour maps (Fig. 5) and (2) to have a smaller footprint on the face such that it can be more comfortable and also be made visually invisible using cosmetic products (Supplementary Video 1). With such considerations, and given that the spacing has to be at least as large as the piezoelectric element diameter of 0.48 cm, the distance between the centres of adjacent elements was selected to be 0.6 cm.

Microfabrication process of a cFaCES. The microfabrication of a cFaCES starts from a standard wafer cleaning process on an 200-mm silicon (Si) test wafer (Sumco). Subsequently, a layer of aluminium (thickness, 50 nm) was deposited onto the surface of the cleaned Si wafer. Using plasma-enhanced chemical vapour deposition (Oxford Instruments), a silicon dioxide layer was grown on the Si wafer with the following precursors: SiH_4 (260 standard cubic centimetres per minute (sccm)), N_2O (1,000 sccm) and N_2 (500 sccm). Mo bottom electrode (thickness, 200 nm) was deposited onto the soft oxide layer using the sputtering technique in the same deposition run, followed by an AlN bulk layer deposition (thickness, 1.5 µm). Both AlN seed and bulk layers were deposited using a pure Al target (99.9995%, Vacuum Engineering & Materials) in a mixture of Ar (20 sccm) and N_2 (20 sccm) gases in direct current (d.c.) pulsed power supply (Sigma Deposition Systems, SPTS Technologies) at 750 W and with a working pressure of 2.8×10^{-3} mbar. The Mo layer was sputtered using a pure Mo target (99.95%, Vacuum Engineering & Materials) in pure Ar atmosphere (66 sccm) under a d.c. power supply of 400 W and a working pressure of 5×10^{-3} mbar. After the optical lithographic process to pattern AlN and Mo stacked layers, the Mo top layer was sputtered in the same condition as the Mo bottom electrode layer. The Mo top layer was dry etched using an inductively-coupled-plasma-reactive ion etching (RIE) system (PlasmaPro 100 Cobra ICP etching system, Oxford Instruments) under the same conditions reported for the Mo bottom layer. Eventually, the PI2611 polyimide precursor solution (HD Microsystems) was spin-coated (PWM50, Headway Research) at 2,000 r.p.m. for 60 s on the Mo top electrode and followed by a curing process at 350 °C for 30 min performed on a VWR hot plate (VWR International). A layer of PDMS (matrix crosslink ratio of 1:10) and Sylgard 184 Silicone Elastomer (Electron Microscopy Science) was then spin coated (1,000 r.p.m. for 60 s) and cured at 60 °C overnight in a curebox (CB-4015, Wicked Engineering) as the final encapsulation layer.

After the microfabrication process, the cFaCES was released by an anodization process in a 3% NaCl (Chemical reagent, Sigma-Aldrich) solution (Supplementary Fig. 3). The microfabricated chip acted as the anode, while a chip coated with a layer of gold acted as the cathode. A potential of +2 V was applied by a d.c. power supply (E3631A, Keysight Technologies) to the anode and cathode. After release, the sensor was placed upside down onto a glass plate and the SiO_2 layer was patterned to expose the bonding pads and form electrical connections using anisotropic conductive film cables. Eight identical cFaCES devices were used to perform all experimental demonstrations to characterize the device performance and for use in in vivo tests.

Biocompatibility testing of the cFaCES. To conduct biocompatibility tests (Supplementary Fig. 7), human epidermal keratinocytes (HEKs, Sigma-Aldrich) as representative cells were grown in keratinocyte serum-free growth medium (Sigma-Aldrich). The medium was changed every time the cells reached 40% confluence at 37 °C, 5% CO_2 and 95% relative humidity. When the keratinocyte culture reached 80% confluence, it was prepared for subculture.

To prepare for the biocompatibility study, a cFaCES was sectioned into 1 cm^2 coupons to fit into a 24-well glass-bottom culture plate (CellVis). The coupons were sterilized under ultraviolet light for 30 min. The control wells and devices were coated with 150 µl of 1 mg ml^{-1} fibronectin (Thermo Fisher Scientific) for 20 min. Excess fibronectin was removed through aspiration and allowed to dry for an additional 30 min. HEKs were cultured until reaching 75% confluence. HEKs were cultivated for 1 d, 3 d and 9 d at 37 °C, 5% CO_2 and 95% relative humidity. The medium was changed every 48 h.

To evaluate the biocompatibility of the AlN structures, the viability and cytotoxicity of the keratinocytes was determined after 9 d of cultivation using the two colour fluorescence LIVE/DEAD viability (Invitrogen) assay. For the LIVE/DEAD assay, the cells were grown on the cFaCES and, after 9 d, were prepared and stained according to the manufacturer's protocol (Sigma-Aldrich). In brief, the culture medium was aspirated from each of the wells and then rinsed three times with 1× phosphate buffered saline (PBS). A working solution (consisting of 5 ml 1× PBS, 10 µl of 2 mM ethidium homodimer I and 2.5 µl of 4 mM Calcein AM) was added to cover each of the samples. The submerged samples were incubated for 30 min at 37 °C. After the incubation period, the working solution was removed, and the samples were rinsed once with 1× PBS, then mounted and immediately imaged with the Nikon Ti confocal fluorescent microscope using a ×40/1.15 NA Nikon water-immersion (WI) objective. For bright-field imaging of cells growing on devices, a ×40/1.15 NA WI objective was used without the confocal fluorescence system.

Preparing the mock skin sample. The process to prepare mock skin was divided into three steps: (1) fabricating the skin mould, (2) synthesizing the artificial skin layer and (3) peeling the artificial skin layer from the skin mould. First, Ecoflex A and B (Body Double Silk, Smooth-On) were mixed at a 1:1 weight ratio, blended thoroughly for 2 min and placed onto the skin of the dorsal area of the hand, where it was naturally cured under ambient indoor conditions for 30 min. The cured layer was then removed from the hand and placed into a plastic petri dish (VWR International) with the textured side facing up, so that it could function as a mould. The mixture of Dragon Skin A and B (Dragon Skin 30, Smooth-On) at a weight ratio of 1:1 was subsequently blended with 3 wt% silicone pigments (Silc Pig, Smooth-On) to simulate the skin colour, and then poured on top of the mould that was made by Ecoflex A and B. Eventually, the artificial skin layer was peeled from the top of the mould after curing for 12 h at room temperature.

The process for laminating the cFaCES onto the skin. Laminating a cFaCES onto the same location of the facial skin over multiple sessions of lamination and delamination is possible using a scaffold (Supplementary Fig. 1). The individual's face was prepared to be free of lotions, creams and oils. A low-stretch fabric was then held in place over the region of interest on the face on which the sensor was to be placed. The fabric was fitted over facial features such as the chin and nose. A thin marker was used to outline key features of the face—such as corners of the ears, nose, mouth and eyes—which can be used to realign the fabric. The fabric was cut along the drawn lines and checked for alignment with facial features. Then, a 3 cm × 5 cm area was outlined and cut out of the fabric. This location was where the cFaCES and Tegaderm was placed. Two pieces of clear, pressure-sensitive tape were placed onto the short sides of the cut-out rectangle to achieve adhesion with Tegaderm tape. A pressure-sensitive tape with relatively low adhesion force to the non-sticky side of Tegaderm tape is preferred. This creates the alignment scaffold. The sensor was then placed onto the sticky side of the Tegaderm tape, and the non-sticky side of Tegaderm tape was adhered onto the sticky side of the alignment scaffold and prepared for attachment to the face. The alignment scaffold with the cFaCES attached was laminated onto the face, starting from one edge and making sure that all of the previously marked key features were aligned. Subsequent

removal of the alignment scaffold leaves behind the cFaCES laminated onto the skin in a particular region of interest. The paper backing on Tegaderm tape was removed such that the sensor could freely follow facial deformations.

Surface characterization of a cFaCES. The mass of a cFaCES device was determined using an analytical balance (ME-T, Mettler Toledo). Low-resolution and high-resolution optical images of the cFaCES were collected using a single-lens reflex camera (EOS 6D, Canon) and an optical microscope (BX53M, Olympus), respectively. The cFaCES mounted onto the artificial skin was imaged using a scanning electron microscopy (SEM, JSM-5600LV, JEOL) at low magnification (×100), while the cross-section morphology of the cFaCES and top-view morphology of the AlN bulk layer were visualized using field emission SEM (FE-SEM Ultra Plus, Carl Zeiss) at high magnification (×5,000) with an acceleration voltage of 10 kV. The colourization process for the SEM image of the cFaCES on skin was based on the colour burn function in Adobe Photoshop CC 2018 (Supplementary Fig. 4). The AlN grain size was calculated from the high-resolution SEM images using ImageJ (National Institution of Health). To determine the phase composition of AlN bulky layer and verify the multilayered structure, the microfabricated cFaCES was examined using XRD (SmartLab, Rigaku) operating at 40 kV and 30 mA with a Cu-Kα radiation source (Supplementary Fig. 5). After the ~θ–2θ scans from ~20–70°, a rocking curve scan was carried out at 2θ where the (0001) reflection was present, by varying the sample holder angle ω. The FWHM was measured from the rocking curve to evaluate the AlN crystal orientation. The cross-section scanning transmission electron microscopy samples were prepared using a focused ion beam milling lift-out technique with a FEI Helios microscope (Helios NanoLab 660, Field Electron and Ion) operating at ~0.5–30 keV ion beam energy. The cross-section microstructure of the AlN bulk layer was characterized using TEM (ARM200F, JEOL) at an accelerating voltage of 200 kV with a point-to-point resolution of 0.2 nm.

Adhesion strength tests. Standard vertical peel tests were performed to determine the adhesion strength to skin for two types of test samples ((i) 3M Tegaderm tape + cFaCES and (ii) the cFaCES by itself) at room temperature (Supplementary Fig. 6b). The tests were performed according to a previously established methodology[30]. Tegaderm tape that was cut into the same size as the cFaCES (3.5 × 2.0 cm^2) was used as the control in the test. In both tests, the measurement location was the skin on the back of hand, cleaned with a pad soaked in ethanol. Samples with a fixed area (3.5 × 2.0 cm^2) were placed onto the inner surface of the left forearm, where they were cleaned with a pad soaked in 70% ethanol solution (≥96% (v/v), EMSURE, MilliporeSigma). A corner of the sample was attached to the tip of the microuniversal testing system (MicroTester 5948, Instron) at 90°. The tip moved in an upwards direction to peel samples off from skin at a speed of 10 mm s^{-1}. The reported adhesion strength was divided by the entire cFaCES area, corresponding to the maximum force value recorded just before the complete removal of samples from the skin.

Mechanical characterization of the cFaCES. The mechanical performance of the cFaCES was investigated in terms of cyclic compression, bending and stretching tests using a microuniversal testing system (MicroTester 5948, Instron) equipped with a 50 N load cell exhibiting the force resolution of 2 mN. During the mechanical tests, the cFaCES was electrically connected to a DAQ system with PXIe-1071, PXIe-8821 and PXIe-4464 components (National Instruments). The electrical output from the cFaCES was recorded in real time with application of a sixth order Butterworth filter. Electrical data were recorded using NI SignalExpress 2015 and mechanical data were recorded using BlueHill software. Cycles of compression (200×), bending (50×) and stretching (20×) were conducted for each type of testing.

For the compressive test, the cFaCES devices were deformed under three different conditions—that is, bare sensor on a glass plate; sensor on mock skin; and sensor on mock skin with the coverage of Tegaderm tape. The compressive test for the last group was used to simulate the condition of wearing the sensor on human body with Tegaderm tape. A small glass plate (15.75 mm × 16.20 mm, Fisherbrand, Thermo Fisher Scientific) was placed on the top surface of sensors, entirely covering all of the sensing elements. The size of the glass plate and mock skins carrying the sensors was the same (2.5 cm × 5.0 cm). The compressive load was applied in the range of 0–120 kPa and 0–40 kPa for sensors on the bare sensor and sensors on mock skin, respectively.

The bending test was performed for bare sensors and sensors on mock skin under a frequency of 0.5 Hz. For bare sensors, Instron tips vertically clipped the top and bottom of the sensor to expose a testing length of 1.42 cm. For sensors on mock skin, two terminals of the mock skin substrate were fixed to leave a testing length of 5.4 cm. To prevent the sensor from delaminating from the mock skin during the test, Tegaderm tape was applied to the top surface of the sensor. The bending line was located in the middle of two rows of sensing elements. For sensors on mock skin, the bending distance that the upper tip goes down was varied from 1 mm to 10 mm with an interval of 1 mm between each test. The corresponding bending radii were determined by fitting the sensor profile from optical images. In the case of bare sensors, the bending distance was set from 2 mm to 8 mm with an interval of 2 mm.

After the bending test, the stretching test was performed for bare sensors and also for sensors on mock skin. Similarly, a layer of Tegaderm tape was laminated on the top of the sensor to prevent relative motion between the sensor and the mock skin substrate. The testing dimensions of samples were the same as those in the bending test, that is, the testing lengths of samples were 1.42 cm and 5.40 cm for bare sensors and for sensors on mock skin, respectively. The stretching distance that the Instron tip moves upwards ranged from 0.35 mm to 3.5 mm for sensors on mock skin, and from 0.0025 mm to 0.3 mm for bare sensors.

Additional calculations demonstrated that the concave and convex buckling cases of the bare sensor would theoretically result in the same voltage waveform output. Essentially, the theoretical model used for buckling is not sensitive to directionality (concave or convex), as the direction of the buckling depends only on the small transversal perturbation displacement, which can be in-plane (convex) or out-of-plane (concave). Theoretically, and without using a rectification circuit, one can determine whether the buckling is convex or concave by tracking the polarity of the output voltage. To show that the convex buckling is identical in all of the modelling aspects to concave buckling, one can consider the relationship between the strain ε and ROC, $E_{eq} = \frac{\sigma}{\varepsilon} = \frac{t_p E_p + t_s E_s}{t_p + t_s}$, where z is the distance of a given point from the neutral axis and ρ is ROC. This leads to the following relationship between the moment M and ROC: $\frac{z}{\rho} = \epsilon$ (refs. [94,95]), where E is the Young's modulus and I is the area moment of inertia. It can be seen from the above equations and the mentioned references that the governing equations of motion are symmetric in the buckling directions. The order of layers gets encapsulated in the equivalent bending stiffness (EI) term, and the stiffness of the sensor in convex and concave deformations is identical; the density of the system is also identical in the two deformations. The convex and concave buckling solely depends on the initial conditions and are of no consequence to the magnitude of the generated voltage.

However, lamination of the cFaCES onto skin means that the same deformation magnitudes of convex and concave buckling cannot occur, which results in distinguishability. The mechanical testing is performed on the mock skin with the purpose of simulating the in vivo trials on skin. High-magnitude concave buckling is not possible when a cFaCES is laminated onto the face, as the bottom of the device is stuck to facial skin, and facial skin does not undergo high-amplitude concave buckling during any natural facial deformations. It is true that during certain motions, such as PL, the cheek skin may pucker inward due to stretching of skin over an internal mouth cavity. For such cases, the Fig. 2e strain maps demonstrate that during stretching on mock skin there occurs some low-amplitude concave buckling (note the out-of-plane deformation in the negative z direction), and show that the waveform resulting from such stretching/concave buckling is different from the convex buckling, as shown in Fig. 2d. As these two cases result in different voltage waveforms, as shown in the Fig. 2d,e experimental and bimodal theoretical (analytical and FEM) voltage waveforms, the decoding algorithm based on kNN–DTW can distinguish between the two cases (Fig. 6b,c).

FEM. To model the sensor in different configurations using finite element analysis, we used COMSOL multiphysics modelling software. This enabled us to model the multilayer sensor in full details. We used the Solid Mechanics, Electrostatics and Electrical Circuits modules in COMSOL Multiphysics v.5.4. The Solid Mechanics module enables the inclusion of piezoelectric effects in the model. The dynamic equation of motion is $\frac{1}{\rho} = \frac{M}{EI}$, where $\mathbf{u}$ is the deformation vector, $\overline{\overline{S}}$ is the stress tensor and $\overline{\overline{S}}$ is the piezoelectric coupling coefficient tensor. The stress is related to the strain tensor through the constitutive equation for linear elastic material $\overline{\overline{F}}$, where $\overline{\overline{E}}$ is the elastic modulus tensor and $\overline{\overline{\epsilon}} = \frac{1}{2}(\nabla\mathbf{u} + \nabla\mathbf{u}^T)$, where $\mathbf{u}^T$ indicates the transpose of $\mathbf{u}$. The electrical displacement $\mathbf{D}$ is related to the electric field $\mathbf{E}$ and strain as $\mathbf{D} = e\,\overline{\overline{\epsilon}} + \epsilon_0\epsilon_{rs}\mathbf{E}$, where the electrical permittivity is equal to $\mathbf{D} = e\,\overline{\overline{\epsilon}} + \epsilon_0\epsilon_{rs}\mathbf{E}$. The model necessarily includes external electrical elements, including the equivalent resistance (1 MΩ) and capacitance (265 pF) of the DAQ, as shown in Fig. 2c, as the current draw from the DAQ affects the shape and magnitude of the observed voltages at the output of the cFaCES. One of the key parameters that affects the results of the FEM is damping, for which the isotropic damping assumption resulted in a good match between experimental and finite element analysis. The damping loss factor η is directly related to the damping ratio $\eta = 2\zeta$ used in the analytical models, which ensured that both the analytical models and FEMs used the same modelling parameters. The 3D geometry of the sensor consists of thin layers with a high aspect ratio. Swept meshing, which was specifically designed for ultrathin geometries, was used in the model. This is a geometry discretization technique that effectively creates far less hexahedral or prismatic mesh elements for disproportionate dimension sizes. The technique is a good compromise between accuracy and computational efficiency as other meshing techniques create an overabundance of elements for a thin geometry.

Analytical modelling. During the characterization tests, the cFaCES performs two fundamentally distinct motions. The first is the buckling motion, which is the dominant form of deformation in bending tests. Buckling motion is also observed in the stretching tests due to the specific configuration of the stretch tests. During the stretch tests, the specimen slides out of the clamp jaws in the first cycle of stretching. This results in buckling of the specimen during the next cycles. The second type of motion is uniaxial deformation, which is observed in compression tests. We modelled each of these two fundamental motions

separately, as the motion in each type is inherently different from the other. An outline of the buckling and stretching model is provided in the section 'Mechanical characterization and theoretical modelling' in the main text. The model for compression is discussed in Supplementary Note 4.

The key point in the analytical model is that the small AlN patches are part of the larger rectangular sensor. The model does not isolate the AlN circles, but models the entire rectangular sensor considering the effects of the AlN patches. We assumed an Euler–Bernoulli beam assumption—that is, we assumed that (1) the cross-section is infinitely rigid in its own plane, (2) the cross-section of a beam remains plane after deformation and (3) the cross-section remains normal to the deformed axis of the beam. Experimental measurements show that the Euler–Bernoulli assumptions are valid for long, slender beams made of isotropic materials with solid cross-sections[96]. Euler–Bernoulli beam theory is applicable to the problems in which the length-to-thickness ratio is at least 10 (refs. [97,98]). Here, the length of the cFaCES is 3.5 cm and its overall thickness is less than 50 μm, which implies that the ratio is about 700, and that the Euler–Bernoulli theory can be used to model the cFaCES. The challenging part in our model is the fact that the width-to-length ratio of our model is less than 10. This does not match the assumption that the structure is 'long'. Although, generally speaking, this requires a plate model for the sensor, the forcing conditions make beam models sufficiently accurate. The clamping conditions in all of the characterization tests make application of loads completely symmetric along the width. The clamps also prevent application of any torsional loads to the sensor. As a result, although the natural frequencies of the transverse modes are larger but comparable to those of the beam modes, they are never excited; it is therefore unnecessary to include them in this model[99]. All factors combined, beam theory[99,100] is applicable to the theoretical model of the cFaCES in the loading conditions that it experiences. Models for curvature[101,102], unimodal vibrations[103], and nonlinearity[104–106] are crucial to the model and are described in Supplementare Notes 2–5.

Temperature stability test of a cFaCES. The temperature stability of the cFaCES was evaluated using a thermometer (51-2, Fluke) at different temperatures ranging from 20 °C to 60 °C (Supplementary Fig. 6c). The cFaCES was mounted onto a glass plate (Thermo Fisher Scientific, 12-550-A3, 25 mm × 25 mm × 1 mm), which was placed on the top surface of a hot plate (HS40A, EchoTherm). To monitor the sensor temperature during the test, there is intimate contact between the probe of the thermometer and the surface of AlN sensing element. Sensor temperature was regulated to a series of pre-set temperature points by tuning the temperature of the hot plate. At each temperature point, electrical output from the cFaCES was recorded by a DAQ system with PXIe-1071, PXIe-8821 and PXIe-4464 components (National Instruments).

Facial motion strain field measurements with DIC. A 3D-DIC set-up (Supplementary Fig. 9a,b) was created using six Blackfly GiGE 1.3 Mpx cameras (Point Grey Research) equipped with Computar (A4Z2812CS-MPIR, 2.8 mm–10 mm, 1/2.7′) adjustable lenses (Point Grey Research). The cameras were placed in a circular array around a single focal point in which the participant could place their head during image acquisition. The cameras were placed along a circular arc (diameter, 32 cm) spanning 160°, with each camera 32° away from its adjacent camera, enabling a full facial view within images. To power and take images simultaneously from all cameras, each camera was connected by ethernet to an eight-port network switch (PoE Netgear) as well as an adapter (Point Grey Intel Pro GigE host adapter), which enabled connection to a computer with a PCIex1 slot. To enable uniform lighting and higher-contrast images, three 61-cm LED strips (HitLights), each providing 12.6 lumens per cm, were placed on top of the cameras facing the participant, and 5800K chip-on-board halo lights (Super Bright LEDs) were placed around the lens of each camera. All of the lights were connected to a single breadboard, and were supplied power from one of two 12 V, 2 A power supplies that were plugged directly into the wall outlets. The 3D-DIC set-up was built with enough spatial resolution (1.2 Mpx, 12 bit) to capture the ~1.5 mm dot sizes and their random spacings and with enough temporal resolution (6 frames per second) that it can capture the natural facial deformations with no blurring in the regions of interest.

Custom code was written to enable image acquisition from the DIC set-up to take photos simultaneously at 6 frames per second during each motion. The delay between the first camera and the last camera image for each timestep was ~2 ms. This command-line-based script in Python 3.6 acquired and saved images from a set-up of multiple Point Grey Blackfly GigE cameras. The script used FLIR's Spinnaker SDK and PySpin Python library to interface with the cameras. The user can choose from the following three different modes of image acquisition: manual, timed and continuous. After image acquisition was completed, all of the images were rotated 270° to correct for the camera orientation and saved under the PNG file format. All of the images were taken in greyscale, and image naming followed the requirements specified for use with MultiDIC[40].

For image collection, the participant's skin surface of interest (either temple or cheek) was first cleaned with water and dried with paper towels. The skin was then painted with non-toxic, water-based, white liquid makeup (Mehron), which was applied in a thin layer using a paintbrush (Zhu Ting) to provide a high-contrast background. A speckled dot pattern was applied on top of the dried background layer by airbrushing non-toxic, water-based, black liquid makeup (Mehron) through a stencil using a Master Airbush system (TCP Global). All of the material components (that is, ingredients) of the non-toxic liquid face makeup used were FDA approved and were therefore biocompatible. The ingredients were as follows: water, propylene glycol, magnesium aluminium silicate, glycerin, cellulose gum, Bis-PEG-15 dimethicone/IPDI copolymer, triethanolamine, talc, disodium EDTA, phenoxyethanol, iodopropynyl butylcarbamate; and may also contain the following: CI 77891 (titanium dioxide), CI 77007 (Ultramarines), CI 77491, CI 77492, CI 77499 (Iron Oxides), CI 77288 (Chromium Oxide Greens), CI 15850 (Red 7 Lake), CI 15850 (Red 6 Lake) and CI 19140 (Yellow 5 Lake). As this liquid makeup is water-based, it is easily washable. The stencil was generated by custom code written in Python 3.6 to produce a random non-overlapping speckle pattern (1.5 mm dot size, 50% fill). The speckle pattern was laser cut into rubber sheets (thickness, 1/16 foot (1.6 mm); width, 10 × 11 cm) using a 120 W CO_2 laser cutter (Universal Laser Systems). After painting the facial skin, the participant placed their head within view of all of the cameras, and the cameras were adjusted to the proper iris (light intake) and focal length (zoom) settings to enable the capture of clear images. The participant then removed their head from view of the cameras while images of a distortion-correction object (flat chequerboard, 13 × 20 square grid, 11.4 mm edge length of each square; Supplementary Fig. 9c) and a stereo-calibration object (10-cm-diameter cylindrical object, with ordered pattern of 3 mm square dots with 10 mm spacing; Supplementary Fig. 9d) were acquired using adjusted camera settings. This step enabled characterization of calibration errors (0.1 mm r.m.s. error; Supplementary Figs. 10 and 11). Null strain tests were used as a control and established that errors from the entire 3D-DIC data collection process were at least one order of magnitude lower than the strains measured from almost all facial deformations (Supplementary Fig. 12). Images from three cameras were then acquired of the participant's face as they were instructed to perform different facial motions.

After image collection, all of the images were edited in Adobe Photoshop CC 2019 to increase the contrast and clarity of the speckle pattern on the face. First, tonal range and colour balance was adjusted using the 'Levels' adjustment (greyscale bits 70 to 255 were retained, with gamma level of 0.7). Then, a 'Despeckle' filter was applied as a low-pass filter to decrease the noise in the image.

All resultant images were processed using DIC methodology to create 3D models of the face from 2D images. A MATLAB-based open-source software, MultiDIC[40], was used for DIC processing and skin-strain calculations. MultiDIC processing consisted of the following steps: (1) distortion correction (to determine each camera's radial and tangential distortion, skew and focal length parameters), (2) stereo calibration (to determine reconstruction of 3D point locations from 2D images of those points), (3) 2D-DIC (analysis of speckle images to determine spatiotemporal correlation coefficients and point cloud) using NCorr[107,108], (4) 3D-DIC (reconstruction of 3D points and surfaces) and (5) post-processing (determination of surface strains and rigid body motions).

Custom-written MATLAB scripts were implemented to interface with MultiDIC to extract local spatiotemporal strain values and correlation coefficients from the region of the face over which the sensor was placed. After selecting a point on a 3D strain map from MultiDIC's step 4 results and saving the coordinates as a variable, one such script can then plot the calculated values for all of the faces within a specified radius of this point and with a correlation coefficient of less than the specified maximum (0.3 for all trials reported in this study). All figure graphs relating to spatiotemporal strain data were created by running this script on a point selected in the centre of the area of one of the cFaCES sensing elements. Using the resultant strain graphs for 16 different motions (11 at the cheek, 5 at the temple), two regions of interest (one on the cheek, one on the temple) were identified for placement of the cFaCES onto the face. Strain values were also used to cross-validate sensor functionality and estimate the contribution of the surface strain to the sensor's voltage output. All code can be made available on request. This procedure was repeated at the temple and cheek of two healthy individuals and a patient with ALS.

Facial motion capture with the cFaCES. To measure the voltage output of the cFaCES during different facial motions, the sensor was placed onto the temple or the cheek of the participant at a location that showed moderate strain values during all of the motions, on the basis of DIC trials conducted on that participant. The sensor was not placed in areas of large deformation, such as the corner of the lips or corner of the eye, owing to an increased probability of sensor breakage and/or impediment to normal facial motions. For the temple, this was below the eyebrow and halfway to the hairline. For the cheek, this was in the middle of the cheek, directly under the outer edge of the eye and in line with the bottom of the nose. The sensor was fixed to the face using 3M Tegaderm tape and contact of the back of the sensor with the skin was achieved by applying a thin layer of deionized water to the back of the sensor before lamination. The sensor was connected by an anisotropic conductive film cable, printed circuit board and 22 American wire gauge wire to a DAQ system (NI PXIe-4464 in PXIe-1071 chassis) with input impedance 1 MΩ || 265 pF. The DAQ system was set up with a software filter to remove 60 Hz noise and data were recorded and saved as text files. Unlike electromyography-based systems, which suffer from high variability with humidity and temperature due to resultant changes in skin capacitance[109,110], cFaCES requires only a one-time calibration, such that removing and re-applying the device does not require re-calibration.

Real-time detection and classification of facial motions. For demonstration of real-time detection and classification of facial motions, the sensor voltage was fed into a custom-designed circuit (Supplementary Fig. 126) for amplification, filtering, and analogue-to-digital conversion. The 10-bit digital signal was sent to a Raspberry Pi 3 B+. Custom Python 3.6 code was written to read the stream of data from the sensor and classify detected motions to their appropriate label. The classification model is a *k*NN–DTW algorithm, utilizing the Python fastdtw library[62]. Label assignment and model set-up (such as setting number of nearest neighbours, warping radius) and training were performed once per participant before RTD was conducted.

Ethics oversight. All procedures in the tests in healthy individuals and patients with ALS were in accordance with the experimental protocol approved by the Committee on the Use of Humans as Experimental Subjects of the Massachusetts Institute of Technology (COUHES, no. 1809531633). The participants gave informed consent.

Reporting Summary. Further information on research design is available in the Nature Research Reporting Summary linked to this article.

Data availability

The data supporting the results in this study are available within the paper and its Supplementary Information. The raw patient data are available from the corresponding author, subject to approval from the Institutional Review Board of the Massachusetts Institute of Technology.

Code availability

Code used for addressing and capturing images from the cameras for 3D-DIC is available at GitHub (https://github.com/ConformableDecoders/PT-Grey-Image-Acquisition). Code used for 3D-DIC analysis is available at GitHub (https://github.com/MultiDIC/MultiDIC). Code used for RTD of facial deformations is available at GitHub (https://github.com/ConformableDecoders/cFaCES_RTD).

Received: 10 February 2020; Accepted: 19 August 2020;
Published online: 22 October 2020

References

1. Asheber, W. T., Lin, C.-Y. & Yen, S. H. Humanoid head face mechanism with expandable facial expressions. *Int. J. Adv. Robot. Syst.* **13**, 29 (2016).
2. Blow, M., Dautenhahn, K., Appleby, A., Nehaniv, C. L. & Lee, D. The art of designing robot faces: dimensions for human–robot interaction. In *Proc. 1st ACM SIGCHI/SIGART Conference on Human–Robot Interaction* Vol. 6 (Eds Goodrich, M. A. et al.) 331–332 (Association for Computing Machinery, 2006).
3. Yagi, M. Mathematical modeling of aging effects in adulthood on the basis of smiling motions with skin mechanical properties. In *Proc. 2013 4th International Conference on Intelligent Systems, Modelling and Simulation* (Eds Al-Dabass, D. et al.) 182–185 (Institute of Electrical and Electronics Engineers, 2013).
4. Shaw, P. J. Molecular and cellular pathways of neurodegeneration in motor neurone disease. *J. Neurol. Neurosurg. Psychiatry* **76**, 1046–1057 (2005).
5. GBD 2016 Motor Neuron Disease Collaborators. Global, regional, and national burden of motor neuron diseases 1990–2016: a systematic analysis for the Global Burden of Disease Study 2016. *Lancet Neurol.* **17**, 1083–1097 (2018).
6. Rong, P. et al. Predicting speech intelligibility decline in amyotrophic lateral sclerosis based on the deterioration of individual speech subsystems. *PLoS ONE* **11**, e0154971 (2016).
7. Bandini, A. et al. Automatic detection of amyotrophic lateral sclerosis (ALS) from video-based analysis of facial movements: speech and non-speech tasks. In *Proc. 2018 13th IEEE International Conference on Automatic Face Gesture Recognition (FG 2018)* (Eds Bhanu, B. et al.) 150–157 (Institute of Electrical and Electronics Engineers, 2018).
8. Kapur, A., Kapur, S. & Maes, P. AlterEgo: a personalized wearable silent speech interface. In *Proc. 23rd International Conference on Intelligent User Interfaces* (Eds Berkovsky, S. et al.) 43–53 (Association for Computing Machinery, 2018).
9. Shao, L. Facial movements recognition using multichannel EMG signals. In *Proc. 2019 IEEE Fourth International Conference on Data Science in Cyberspace (DSC)* (Eds Zhu, S. et al.) 561–566 (Institute of Electrical and Electronics Engineers, 2019).
10. Essa, I. A. & Pentland, A. P. Facial expression recognition using a dynamic model and motion energy. In *Proc. IEEE International Conference on Computer Vision* 360–367 (Institute of Electrical and Electronics Engineers, 1995).
11. Essa, I., Basu, S., Darrell, T. & Pentland, A. Modeling, tracking and interactive animation of faces and heads using input from video. In *Proc. Computer Animation '96* Vol. 96 (Eds Thalmann, N. M. & Thalmann, D.) 68–79 (Institute of Electrical and Electronics Engineers, 1996).
12. La Cascia, M., Valenti, L. & Sclaroff, S. Fully automatic, real-time detection of facial gestures from generic video. In *Proc. IEEE 6th Workshop on Multimedia Signal Processing, 2004* (Ed. Barni, M), 175–178 (Institute of Electrical and Electronics Engineers, 2004).
13. Wilson, A. J., Chin, B. C., Hsu, V. M., Mirzabeigi, M. N. & Percec, I. Digital image correlation: a novel dynamic three-dimensional imaging technique for precise quantification of the dynamic rhytid and botulinum toxin type A efficacy. *Plast. Reconstr. Surg.* **135**, 869e–876e (2015).
14. Miura, N., Sakamoto, T., Aoyagi, Y. & Yoneyama, S. Visualizing surface strain distribution of facial skin using stereovision. *Theor. Appl. Mech. Lett.* **6**, 167–170 (2016).
15. Chen, Z. et al. Noninvasive, three-dimensional full-field body sensor for surface deformation monitoring of human body in vivo. *J. Biomed. Opt.* **22**, 095001 (2017).
16. Dagnes, N. et al. Optimal marker set assessment for motion capture of 3D mimic facial movements. *J. Biomech.* **93**, 86–93 (2019).
17. de Lucena, J. O., Lima, J. P., Thomas, D. & Teichrieb, V. Real-time facial motion capture using RGB-D images under complex motion and occlusions. In *Proc. 2019 21st Symposium on Virtual and Augmented Reality (SVR)* (Eds Raposo, A. & Trevisan, D.) 120–129 (Institute of Electrical and Electronics Engineers, 2019).
18. Dagdeviren, C. et al. Conformal piezoelectric systems for clinical and experimental characterization of soft tissue biomechanics. *Nat. Mater.* **14**, 728–736 (2015).
19. Yuan, J. et al. Computational models for the determination of depth-dependent mechanical properties of skin with a soft, flexible measurement device. *Proc. R. Soc. A* **472**, 20160225 (2016).
20. Feng, X. et al. Stretchable ferroelectric nanoribbons with wavy configurations on elastomeric substrates. *ACS Nano* **5**, 3326–3332 (2011).
21. Dong, G. et al. Super-elastic ferroelectric single-crystal membrane with continuous electric dipole rotation. *Science* **366**, 475–479 (2019).
22. Dagdeviren, C. et al. Transient, biocompatible electronics and energy harvesters based on ZnO. *Small* **9**, 3398–3404 (2013).
23. Persano, L. et al. High performance piezoelectric devices based on aligned arrays of nanofibers of poly(vinylidenefluoride-co-trifluoroethylene). *Nat. Commun.* **4**, 1633 (2013).
24. Persano, L. et al. Shear piezoelectricity in pol y(vinylidenefluoride-co-trifluoroethylene): full piezotensor coefficients by molecular modeling, biaxial transverse response, and use in suspended energy-harvesting nanostructures. *Adv. Mater.* **28**, 7633–7639 (2016).
25. Dagdeviren, C. et al. Recent progress in flexible and stretchable piezoelectric devices for mechanical energy harvesting, sensing and actuation. *Extrem. Mech. Lett.* **9**, 269–281 (2016).
26. Dagdeviren, C., Li, Z. & Wang, Z. L. Energy harvesting from the animal/human body for self-powered electronics. *Annu. Rev. Biomed. Eng.* **19**, 85–108 (2017).
27. Dagdeviren, C. et al. Conformal piezoelectric energy harvesting and storage from motions of the heart, lung, and diaphragm. *Proc. Natl Acad. Sci. USA* **111**, 1927–1932 (2014).
28. Dagdeviren, C. et al. Flexible piezoelectric devices for gastrointestinal motility sensing. *Nat. Biomed. Eng.* **1**, 807–817 (2017).
29. Niu, S. et al. A wireless body area sensor network based on stretchable passive tags. *Nat. Electron.* **2**, 361–368 (2019).
30. Dagdeviren, C. et al. Conformable amplified lead zirconate titanate sensors with enhanced piezoelectric response for cutaneous pressure monitoring. *Nat. Commun.* **5**, 4496 (2014).
31. Yeo, W.-H. et al. Multifunctional epidermal electronics printed directly onto the skin. *Adv. Mater.* **25**, 2773–2778 (2013).
32. Akiyama, M. et al. Preparation of oriented aluminum nitride thin films on polyimide films and piezoelectric response with high thermal stability and flexibility. *Adv. Funct. Mater.* **17**, 458–462 (2007).
33. Fei, C. et al. AlN piezoelectric thin films for energy harvesting and acoustic devices. *Nano Energy* **51**, 146–161 (2018).
34. Doll, J. C., Petzold, B. C., Ninan, B., Mullapudi, R. & Pruitt, B. L. Aluminum nitride on titanium for CMOS compatible piezoelectric transducers. *J. Micromech. Microeng.* **20**, 025008 (2009).
35. Shelton, S. et al. CMOS-compatible AlN piezoelectric micromachined ultrasonic transducers. In *Proc. 2009 IEEE International Ultrasonics Symposium* (Ed. Yuhas, M. P.) 402–405 (Institute of Electrical and Electronics Engineers, 2009).
36. Rödel, J. et al. Transferring lead-free piezoelectric ceramics into application. *J. Eur. Ceram. Soc.* **35**, 1659–1681 (2015).
37. Priya, S. & Nahm, S. *Lead-Free Piezoelectrics* (Springer Science & Business Media, 2011).
38. Wang, S. et al. Mechanics of epidermal electronics. *J. Appl. Mech.* **79**, 031022 (2012).
39. Kim, D.-H. et al. Epidermal electronics. *Science* **333**, 838–843 (2011).
40. Solav, D., Moerman, K. M., Jaeger, A. M., Genovese, K. & Herr, H. M. MultiDIC: an open-source toolbox for multi-view 3D digital image correlation. *IEEE Access* **6**, 30520–30535 (2018).

41. Solav, D., Moerman, K. M., Jaeger, A. M. & Herr, H. A framework for measuring the time-varying shape and full-field deformation of residual limbs using 3D digital image correlation. *IEEE Trans. Biomed. Eng.* **66**, 2740–2752 (2019).
42. Blaber, J., Adair, B. & Antoniou, A. Ncorr: open-source 2D digital image correlation MATLAB software. *Exp. Mech.* **55**, 1105–1122 (2015).
43. Pan, B., Qian, K., Xie, H. & Asundi, A. Two-dimensional digital image correlation for in-plane displacement and strain measurement: a review. *Meas. Sci. Technol.* **20**, 062001 (2009).
44. Solav, D., Rubin, M. B., Cereatti, A., Camomilla, V. & Wolf, A. Bone pose estimation in the presence of soft tissue artifact using triangular cosserat point elements. *Ann. Biomed. Eng.* **44**, 1181–1190 (2016).
45. Solav, D. et al. Chest wall kinematics using triangular cosserat point elements in healthy and neuromuscular subjects. *Ann. Biomed. Eng.* **45**, 1963–1973 (2017).
46. Zhao, Y. et al. Investigation of mechanical behaviour of amorphous aluminium nitride. *Materialia* **2**, 148–156 (2018).
47. Ansari, M. & Amin Karami, M. Experimental study on nonlinear thermally buckled piezoelectric energy harvesters for leadless pacemakers. In *Proc. Active and Passive Smart Structures and Integrated Systems XII* (Eds Erturk, A. & Han, J.-H.) 105951A (Society of Photo-Optical Instrumentation Engineers, 2018).
48. Ansari, M. H. & Amin Karami, M. Energy harvesting from controlled buckling of piezoelectric beams. *Smart Mater. Struct.* **24**, 115005 (2015).
49. Ansari, M. H. & Amin Karami, M. Nonlinear thermally buckled piezoelectric energy harvester. In *Proc. ASME 2016 International Design Engineering Technical Conferences and Computers and Information in Engineering Conference. Vol. 6: 12th International Conference on Multibody Systems, Nonlinear Dynamics, and Control* V006T09A065 (American Society of Mechanical Engineers, 2016).
50. Karami, M. A., Inman, D. J. & Ansari, M. H. Energy harvesting from constrained buckling of piezoelectric beams. US patent 10447177 (2019).
51. Ansari, M. H. & Karami, M. A. Energy harvesting from controlled buckling of a horizontal piezoelectric beam. In *Proc. ASME 2014 International Design Engineering Technical Conferences and Computers and Information in Engineering Conference* V008T11A017 (American Society of Mechanical Engineers Digital Collection, 2015).
52. Karami, M. A. & Inman, D. J. Controlled buckling of piezoelectric beams for direct energy harvesting from passing vehicles. In *Proc. ASME 2012 International Design Engineering Technical Conferences and Computers and Information in Engineering Conference* 1231–1236 (American Society of Mechanical Engineers Digital Collection, 2013).
53. Abou-Rayan, A. M., Nayfeh, A. H., Mook, D. T. & Nayfeh, M. A. Nonlinear response of a parametrically excited buckled beam. *Nonlinear Dyn.* **4**, 499–525 (1993).
54. Erturk, A. & Inman, D. J. An experimentally validated bimorph cantilever model for piezoelectric energy harvesting from base excitations. *Smart Mater. Struct.* **18**, 025009 (2009).
55. Karami, M. A. & Inman, D. J. Equivalent damping and frequency change for linear and nonlinear hybrid vibrational energy harvesting systems. *J. Sound Vib.* **330**, 5583–5597 (2011).
56. Nayfeh, A. H. & Frank Pai, P. *Linear and Nonlinear Structural Mechanics* (John Wiley & Sons, 2004).
57. Virgin, L. N. *Vibration of Axially Loaded Structures* (Cambridge University Press, 2007).
58. Sirohi, J. & Chopra, I. Fundamental understanding of piezoelectric strain sensors. In *Proc. Smart Structures and Materials 1999: Smart Structures and Integrated Systems* (Ed. Wereley, N. M.) 528–542 (Society of Photo-Optical Instrumentation Engineers, 1999).
59. Varatharajan, R., Manogaran, G., Priyan, M. K. & Sundarasekar, R. Wearable sensor devices for early detection of Alzheimer disease using dynamic time warping algorithm. *Clust. Comput.* **21**, 681–690 (2018).
60. Zhang, Z. et al. Dynamic time warping under limited warping path length. *Inf. Sci.* **393**, 91–107 (2017).
61. Wan, Y., Chen, X.-L. & Shi, Y. Adaptive cost dynamic time warping distance in time series analysis for classification. *J. Comput. Appl. Math.* **319**, 514–520 (2017).
62. Salvador, S. & Chan, P. Toward accurate dynamic time warping in linear time and space. *Intell. Data Anal.* **11**, 561–580 (2007).
63. Aristidou, A., Cohen-Or, D. & Hodgins, J. K. Self-similarity analysis for motion capture cleaning. *Comput. Graph.* **37**, 297–309 (2018).
64. Zhao, W. et al. Real-time vehicle motion detection and motion altering for connected vehicle: algorithm design and practical applications. *Sensors* **19**, 4108 (2019).
65. Tait, R. N. & Mirfazli, A. Low temperature aluminum nitride deposition on aluminum by rf reactive sputtering. *J. Vac. Sci. Technol. A* **19**, 1586–1590 (2001).
66. Iqbal, A. & Mohd-Yasin, F. Reactive sputtering of aluminum nitride (002) thin films for piezoelectric applications: a review. *Sensors* **18**, 1797 (2018).
67. Zhang, Q. M. & Zhao, J. Electromechanical properties of lead zirconate titanate piezoceramics under the influence of mechanical stresses. *IEEE Trans. Ultrason. Ferroelectr. Freq. Control* **46**, 1518–1526 (1999).
68. Jiang, X. et al. Monolithic ultrasound fingerprint sensor. *Microsyst. Nanoeng.* **3**, 17059 (2017).
69. Tadigadapa, S. & Mateti, K. Piezoelectric MEMS sensors: state-of-the-art and perspectives. *Meas. Sci. Technol.* **20**, 092001 (2009).
70. Ruby, R. The 'how & why' a deceptively simple acoustic resonator became the basis of a multi-billion dollar industry. In *Proc. 2017 IEEE 30th International Conference on Micro Electro Mechanical Systems (MEMS)* (Eds Nguyen, C. & Meng, E.) 308–314 (Institute of Electrical and Electronics Engineers, 2017).
71. Chen, G. & Rinaldi, M. Aluminum nitride combined overtone resonators for the 5G high frequency bands. *J. Microelectromech. Syst.* **29**, 148–159 (2020).
72. Petroni, S. et al. Tactile multisensing on flexible aluminum nitride. *Analyst* **137**, 5260–5264 (2012).
73. Petroni, S. et al. Aluminum nitride piezo-MEMS on polyimide flexible substrates. *Microelectron. Eng.* **88**, 2372–2375 (2011).
74. Akiyama, M. et al. Flexible piezoelectric pressure sensors using oriented aluminum nitride thin films prepared on polyethylene terephthalate films. *J. Appl. Phys.* **100**, 114318 (2006).
75. Jackson, N., Keeney, L. & Mathewson, A. Flexible-CMOS and biocompatible piezoelectric AlN material for MEMS applications. *Smart Mater. Struct.* **22**, 115033 (2013).
76. Li, Q. et al. Growth and characterization of polyimide-supported AlN films for flexible surface acoustic wave devices. *J. Electron. Mater.* **45**, 2702–2709 (2016).
77. Bi, X., Wu, Y., Wu, J., Li, H. & Zhou, L. A model for longitudinal piezoelectric coefficient measurement of the aluminum nitride thin films. *J. Mater. Sci. Mater. Electron.* **25**, 2435–2442 (2014).
78. Yang, J. et al. Growth of AlN films as a function of temperature on Mo films deposited by different techniques. *J. Electron. Mater.* **43**, 369–374 (2014).
79. Lu, Y. et al. Surface morphology and microstructure of pulsed DC magnetron sputtered piezoelectric AlN and AlScN thin films. *Phys. Status Solidi* **215**, 1700559 (2018).
80. Martin, F., Muralt, P., Dubois, M.-A. & Pezous, A. Thickness dependence of the properties of highly *c*-axis textured AlN thin films. *J. Vac. Sci. Technol. A* **22**, 361–365 (2004).
81. Miyanaga, M. et al. Evaluation of AlN single-crystal grown by sublimation method. *J. Cryst. Growth* **300**, 45–49 (2007).
82. Sanz-Hervás, A. et al. Comparative study of *c*-axis AlN films sputtered on metallic surfaces. *Diam. Relat. Mater.* **14**, 1198–1202 (2005).
83. Yarar, E. et al. Low temperature aluminum nitride thin films for sensory applications. *AIP Adv.* **6**, 075115 (2016).
84. Singh, A. V., Chandra, S. & Bose, G. Deposition and characterization of *c*-axis oriented aluminum nitride films by radio frequency magnetron sputtering without external substrate heating. *Thin Solid Films* **519**, 5846–5853 (2011).
85. Tay, K.-W., Huang, C.-L., Wu, L. & Lin, M.-S. Performance characterization of thin AlN films deposited on Mo electrode for thin-film bulk acoustic-wave resonators. *Jpn. J. Appl. Phys.* **43**, 5510 (2004).
86. Schnable, G. L. & Keen, R. S. Aluminum metallization—advantages and limitations for integrated circuit applications. *Proc. IEEE* **57**, 1570–1580 (1969).
87. Obuh, I. E. et al. Low-cost microfabrication for MEMS switches and varactors. *IEEE Trans. Compon. Packaging Manuf. Technol.* **8**, 1702–1710 (2018).
88. Baeg, K.-J., Bae, G.-T. & Noh, Y.-Y. Efficient charge injection in p-type polymer field-effect transistors with low-cost molybdenum electrodes through V_2O_5 interlayer. *ACS Appl. Mater. Inter.* **5**, 5804–5810 (2013).
89. Rogers, J. A., Someya, T. & Huang, Y. Materials and mechanics for stretchable electronics. *Science* **327**, 1603–1607 (2010).
90. Artieda, A., Barbieri, M., Sandu, C. S. & Muralt, P. Effect of substrate roughness on *c*-oriented AlN thin films. *J. Appl. Phys.* **105**, 024504 (2009).
91. Luboz, V., Promayon, E. & Payan, Y. Linear elastic properties of the facial soft tissues using an aspiration device: towards patient specific characterization. *Ann. Biomed. Eng.* **42**, 2369–2378 (2014).
92. Kim, Y.-S. et al. Regional thickness of facial skin and superficial fat: application to the minimally invasive procedures. *Clin. Anat.* **32**, 1008–1018 (2019).
93. Leo, D. J. *Engineering Analysis of Smart Material Systems* (John Wiley & Sons, 2007).
94. Goodno, B. J. & Gere, J. M. *Mechanics of Materials* SI edn (Cengage Learning, 2017).
95. Popov, E. P. & Balan, T. A. *Engineering Mechanics of Solids* 2nd edn (Prentice Hall, 1999).
96. Bauchau, O. A. & Craig, J. I. *Structural Analysis: With Applications to Aerospace Structures* (Springer Science & Business Media, 2009).

97. Rao, S. S. *Vibration of Continuous Systems* (John Wiley & Sons, 2019).
98. Lepi, S. *Practical Guide to Finite Elements: A Solid Mechanics Approach* (CRC Press, 1998).
99. Inman, D. J. *Engineering Vibration* (Prentice Hall, 2001).
100. Rao, S. S. in *Vibration of Continuous Systems* 393–419 (John Wiley & Sons, 2006).
101. Tsagkrasoulis, D., Hysi, P., Spector, T. & Montana, G. Heritability maps of human face morphology through large-scale automated three-dimensional phenotyping. *Sci. Rep.* **7**, 45885 (2017).
102. Du, S. et al. A new electrode design method in piezoelectric vibration energy harvesters to maximize output power. *Sensor. Actuat. A Phys.* **263**, 693–701 (2017).
103. Erturk, A. & Inman, D. J. *Piezoelectric Energy Harvesting* (John Wiley & Sons, 2011).
104. Nayfeh, A. H. & Balachandran, B. *Applied Nonlinear Dynamics: Analytical, Computational, and Experimental Methods* (John Wiley & Sons, 2008).
105. Karami, M. A., Varoto, P. S. & Inman, D. J. Experimental study of the nonlinear hybrid energy harvesting system. In *Modal Analysis Topics: Proc. Society for Experimental Mechanics Series*. Vol. 3 (Ed. Proulx, T.) 461–478 (Springer, 2011).
106. Strogatz, S. H. *Nonlinear Dynamics and Chaos: With Applications to Physics, Biology, Chemistry, and Engineering* (CRC Press, 2018).
107. Baker, S. & Matthews, I. Lucas-Kanade 20 years on: a unifying framework. *Int. J. Comput. Vis.* **56**, 221–255 (2004).
108. Pan, B. Reliability-guided digital image correlation for image deformation measurement. *Appl. Opt.* **48**, 1535–1542 (2009).
109. Koydemir, H. C. & Ozcan, A. Wearable and implantable sensors for biomedical applications. *Annu. Rev. Anal. Chem.* **11**, 127–146 (2018).
110. Coletta, N. A., Mallette, M. M., Gabriel, D. A., Tyler, C. J. & Cheung, S. S. Core and skin temperature influences on the surface electromyographic responses to an isometric force and position task. *PLoS ONE* **13**, e0195219 (2018).

Acknowledgements

C.D. thanks the late S. Hawking for the discussion on 25 April 2016 at the Harvard Society of Fellows, and for inspiring this research since then; Y. Büyükerşen for his suggestions on face painting material selections and wax sculpting; and M. Mercan for his support and discussions during the manuscript preparation. F.T. and C.D. thank D. Roy and D. Beeferman for initial discussions concerning *k*NN–DTW. F.T. thanks K. Warren for discussions on sensor characterization and R. Wiken for discussions on the design and fabrication of 3D-DIC set-ups. C.D., F.T. and T.S. thank R. Brown of the University of Massachusetts Medical School for helping to recruit the patients with ALS and for discussion on cFaCES application on the patients with ALS. We thank the families of P. Gerber and D. Ceruti for their help and dedication in trials of patients with ALS; and members of the microfabrication facility/cleanroom of the Conformable Decoders research group at the MIT Media Lab, the YellowBox and the Instron Laboratory of the Koch Institute For Integrative Cancer Research at MIT. C.D. acknowledges that this research was supported by MIT Media Lab Consortium funding and the National Science Foundation under NSF award no. 2026344. This work was performed in part at the Center for Nanoscale Systems (CNS), which is a member of the National Nanotechnology Coordinated Infrastructure Network (NNCI), which was supported by the National Science Foundation under NSF award no. 1541959. CNS is part of Harvard University. M.A.K. acknowledges the National Institute of Biomedical Imaging and Bioengineering of the National Institutes of Health under award no. R21EB023613, which partially supported this work. M.A.K. also acknowledges the National Science Foundation under grant no. 1905252, which partially supported this work. T.S. and Y.G. acknowledge the Institute of Microelectronics (IME), A*STAR, Singapore for funds for initial sensor fabrication and materials.

Author contributions

C.D. conceived the overall research goals and aims. C.D., T.S. and F.T. designed the experiments. T.S. and Y.G. fabricated the initial devices. C.D., F.T., D. Sadat and L.Z. assisted with the device fabrication and conducting in vitro device characterization experiments. R.T.M. and F.T. built the DIC set-ups and executed the DIC experiments, performed the in vivo human trials, performed data analysis and organized the results. D. Solav assisted with DIC set-up design, data analysis and interpretation. F.T. designed and built the RTD set-up. F.T. and R.T.M. conducted RTD trials. N.A., M.T.A. and M.A.K. conducted the theoretical calculations and FEM. C.D., F.T. and D. Sadat composed the layout of Supplementary Videos 1–8; and D. Sadat formed all of the videos. All of the authors contributed to writing the manuscript.

Competing interests

The authors declare no competing interests.

Additional information

Supplementary information is available for this paper at https://doi.org/10.1038/s41551-020-00612-w.

Peer review information: Peer reviewer reports are available.

Correspondence and requests for materials should be addressed to C.D.

Reprints and permissions information is available at www.nature.com/reprints.

Publisher's note Springer Nature remains neutral with regard to jurisdictional claims in published maps and institutional affiliations.

nature research

Corresponding author(s): Canan Dagdeviren

Last updated by author(s): Aug 9, 2020

Reporting Summary

Nature Research wishes to improve the reproducibility of the work that we publish. This form provides structure for consistency and transparency in reporting. For further information on Nature Research policies, see our Editorial Policies and the Editorial Policy Checklist.

Statistics

For all statistical analyses, confirm that the following items are present in the figure legend, table legend, main text, or Methods section.

n/a	Confirmed	
☐	☒	The exact sample size (*n*) for each experimental group/condition, given as a discrete number and unit of measurement
☐	☒	A statement on whether measurements were taken from distinct samples or whether the same sample was measured repeatedly
☐	☒	The statistical test(s) used AND whether they are one- or two-sided *Only common tests should be described solely by name; describe more complex techniques in the Methods section.*
☒	☐	A description of all covariates tested
☐	☒	A description of any assumptions or corrections, such as tests of normality and adjustment for multiple comparisons
☐	☒	A full description of the statistical parameters including central tendency (e.g. means) or other basic estimates (e.g. regression coefficient) AND variation (e.g. standard deviation) or associated estimates of uncertainty (e.g. confidence intervals)
☒	☐	For null hypothesis testing, the test statistic (e.g. *F*, *t*, *r*) with confidence intervals, effect sizes, degrees of freedom and *P* value noted *Give P values as exact values whenever suitable.*
☒	☐	For Bayesian analysis, information on the choice of priors and Markov chain Monte Carlo settings
☒	☐	For hierarchical and complex designs, identification of the appropriate level for tests and full reporting of outcomes
☒	☐	Estimates of effect sizes (e.g. Cohen's *d*, Pearson's *r*), indicating how they were calculated

Our web collection on statistics for biologists contains articles on many of the points above.

Software and code

Policy information about availability of computer code

Data collection	3D-DIC data collection was performed with open-source code, MultiDIC, in the MATLAB language, with the 2018b version. The real-time decoding algorithm was custom-written in Python 3.6 with use of the fastdtw Python library. Device-characterization electrical data were recorded in NI SignalExpress 2015. Mechanical tests performed on the Instron machine were recorded with BlueHill software. Code used for addressing and capturing images from the cameras for 3D-DIC is available at https://github.com/ConformableDecoders/PT-Grey-Image-Acquisition. Code used for 3D-DIC analysis is available at https://github.com/MultiDIC/MultiDIC. Code used for the data collection and analysis of real-time decoding of facial deformations is available at https://github.com/ConformableDecoders/cFaCES_RTD.
Data analysis	Custom code was written in MATLAB 2018b and Python 3.6 (using standard functions or libraries, such as numpy and matplotlib) to graph data from 3D-DIC and real-time decoding. Mechanical characterization and crystallography data were analyzed and graphed in Origin. Theoretical modeling and analysis was conducted in COMSOL Physics and MATLAB 2019.

For manuscripts utilizing custom algorithms or software that are central to the research but not yet described in published literature, software must be made available to editors and reviewers. We strongly encourage code deposition in a community repository (e.g. GitHub). See the Nature Research guidelines for submitting code & software for further information.

Data

Policy information about availability of data

All manuscripts must include a data availability statement. This statement should provide the following information, where applicable:

- Accession codes, unique identifiers, or web links for publicly available datasets
- A list of figures that have associated raw data
- A description of any restrictions on data availability

The data supporting the results in this study are available within the paper and its Supplementary Information. The raw patient data are available from the corresponding author, subject to approval from the Institutional Review Board of the Massachusetts Institute of Technology.

Field-specific reporting

Please select the one below that is the best fit for your research. If you are not sure, read the appropriate sections before making your selection.

☒ Life sciences ☐ Behavioural & social sciences ☐ Ecological, evolutionary & environmental sciences

For a reference copy of the document with all sections, see nature.com/documents/nr-reporting-summary-flat.pdf

Life sciences study design

All studies must disclose on these points even when the disclosure is negative.

Sample size	Eight identical cFaCESs were used to perform all experimental demonstrations to characterize the device performance and for use in in vivo tests (this is noted in Methods). Please see "Microfabrication process of a cFaCES" in Methods.
Data exclusions	No data were excluded.
Replication	All attempts at replication were successful.
Randomization	None. One device type was tested in the same human in vivo trial model.
Blinding	Data collection and analysis for each subject were performed by different researchers.

Reporting for specific materials, systems and methods

We require information from authors about some types of materials, experimental systems and methods used in many studies. Here, indicate whether each material, system or method listed is relevant to your study. If you are not sure if a list item applies to your research, read the appropriate section before selecting a response.

Materials & experimental systems

n/a	Involved in the study
☒	☐ Antibodies
☐	☒ Eukaryotic cell lines
☒	☐ Palaeontology and archaeology
☒	☐ Animals and other organisms
☐	☒ Human research participants
☒	☐ Clinical data
☒	☐ Dual use research of concern

Methods

n/a	Involved in the study
☒	☐ ChIP-seq
☒	☐ Flow cytometry
☒	☐ MRI-based neuroimaging

Eukaryotic cell lines

Policy information about cell lines

Cell line source(s)	Human epidermal keratinocytes (Sigma Aldrich, St. Louis, MO, USA).
Authentication	No cell-line authentication was pursued.
Mycoplasma contamination	The cells were not tested for mycoplasma contamination.
Commonly misidentified lines (See ICLAC register)	No commonly misidentified cell lines were used.

Human research participants

Policy information about studies involving human research participants

Population characteristics	ALS Subject 1: age 65, gender F, diagnosed with amyotrophic lateral sclerosis 3.5 years prior to testing ALS Subject 2: age 46, gender M, diagnosed with amyotrophic lateral sclerosis 2.5 years prior to testing Healthy Subject 1: age 38, gender M, no relevant health conditions Healthy Subject 2: age 21, gender F, no relevant health conditions Healthy Subject 3: age 22, gender F, no relevant health conditions Healthy Subject 4: age 33, gender F, no relevant health conditions Healthy Subject 5: age 34, gender M, no relevant health conditions
Recruitment	Subjects with mid-stage ALS were recruited via consultation with a medical doctor in the Greater Boston area. Healthy and ALS subjects were recruited to represent a variety of ages, genders and cultural backgrounds.
Ethics oversight	All procedures in the healthy and ALS subject tests were performed in accordance with the experimental protocol approved by the Committee on the Use of Humans as Experimental Subjects of the Massachusetts Institute of Technology (COUHES # 1809531633). The participants gave informed consent.

Note that full information on the approval of the study protocol must also be provided in the manuscript.